Spectra of Saturn's proton belts revealed

Peter Kollmann, Elias Roussos, George Clark, John F. Cooper, Steven J. Sturner, Anna Kotova, Leonardo Regoli, Yuri Y. Shprits, Nikita Aseev, Norbert Krupp

Icarus 376 (2022) 114795

Contents lists available at ScienceDirect

Icarus

journal homepage: www.elsevier.com/locate/icarus

Research Paper

Spectra of Saturn's proton belts revealed

Peter Kollmann [a,*], Elias Roussos [b], George Clark [a], John F. Cooper [c], Steven J. Sturner [c,h], Anna Kotova [d], Leonardo Regoli [a], Yuri Y. Shprits [e,f,g], Nikita Aseev [e], Norbert Krupp [b]

[a] Johns Hopkins University Applied Physics Laboratory, Laurel, MD 20723-6099, USA
[b] Max Planck Institute for Solar System Research, 37077 Göttingen, Germany
[c] NASA Goddard Space Flight Center, Greenbelt MD, USA
[d] IRAP, University de Toulouse, CNRS, UPS, CNES, Toulouse, France
[e] GFZ German Research Centre for Geosciences, Potsdam, Germany
[f] Institute of Physics and Astronomy, University of Potsdam, Potsdam, Germany
[g] Department of Earth, Planetary, and Space Sciences, University of California, Los Angeles CA, USA
[h] University of Maryland, Baltimore County, Goddard Planetary Heliophysics Institute, Baltimore MD, USA

ARTICLE INFO

Keywords:
Radiation belts
Saturn
CRAND
Proton

ABSTRACT

Saturn is permanently surrounded by 6 discrete proton radiation belts that are rigidly separated by the orbits of its inner moons and dense rings. These radiation belts are ideal environments to study the details of radial diffusion and the CRAND source process, yet progress has been hindered by the fact that the energy spectra are not known with certainty: Reanalysis of the response functions of the LEMMS instrument on-board the Cassini orbiter has shown that measurements of $\lesssim 10$ MeV protons may be easily contaminated by $\gtrsim 10$ MeV protons and that many available measurements characterize a very broad energy range, so that the calculation of an energy-resolved spectrum is not as straightforward as previously assumed. Here we use forward modeling of the measurements based on the instrument response and combine this technique where useful with numerical modeling of the proton belt physics in order to determine Saturn's spectra with higher certainty. We find significant proton intensities up to ≈ 1 GeV. While earlier studies reported on proton spectra roughly following a power law with exponent ≈ -2, our more advanced analysis shows harder spectra with exponent ≈ -1. The observed spectra provide independent confirmation that Saturn's proton belts are sourced by CRAND and are consistent with the provided protons being subsequently cooled in the tenuous gas originating from Saturn or Enceladus. The intensities at Saturn are found to be lower than at Jupiter and Earth, which is also consistent with the source of Saturn being exclusively CRAND, while the other planets can draw from additional processes. Our new spectra can be used in the future to further our understanding of Saturn's proton belts and the respective physical processes that occur at other magnetized planets in general. Also, the spectra have applications for several topics of planetary science, such as space weathering of Saturn's moons and rings, and can be useful to constrain properties of the main rings through their production of secondary particles.

1. Introduction

Magnetized planets accumulate radiation belts deep in their magnetospheres. The Earth is surrounded by a single permanent belt of energetic protons, which has a variable outer boundary and can in principle exchange particles with the rest of the magnetosphere (Lorentzen et al., 2002; Selesnick and Albert, 2019). Different to that, Saturn has 6 permanent radiation belts of energetic protons (black curve in Fig. 1, McDonald et al. (1980), Buratti et al. (2019), Roussos et al. (2018b)) that are strictly separated by physical obstacles, namely the orbits of major moons, rings, and Saturn's atmosphere. The concrete obstacles are Saturn itself, the C-A rings, the F ring, Janus, Mimas, Enceladus, and Tethys. They absorb protons that otherwise would be transported radially (Roussos and Kollmann, 2021). There were only a few cases observed where protons populated the orbit of Tethys (Roussos et al., 2018a), otherwise the belts remained unchanged even at times of enhanced magnetospheric dynamics (Roussos et al., 2008).

The absence of coupling of the radiation belts to each other or to the rest of the magnetosphere rules out that they are populated by inward transport of magnetospheric particles. Measurements of protons in the tens of keV energy range show near-zero counts (blue curve in Fig. 1, Krupp et al. (2018a)). Their near-absence suggests that the proton belts cannot originate from locally accelerated low energy

* Corresponding author.
E-mail address: Peter.Kollmann@jhuapl.edu (P. Kollmann).

https://doi.org/10.1016/j.icarus.2021.114795
Received 6 July 2021; Received in revised form 29 October 2021; Accepted 11 November 2021
Available online 24 December 2021

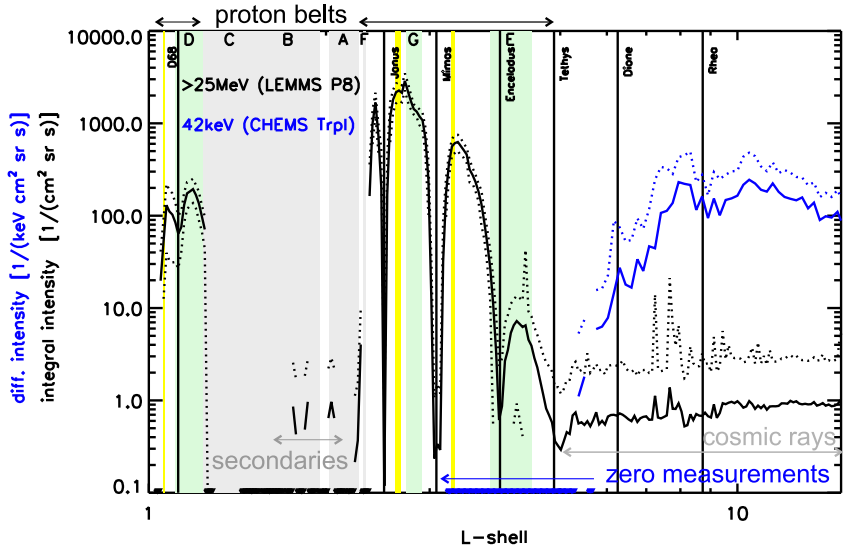

Fig. 1. Solid curves show mission-averaged intensity of energetic protons in Saturn's magnetosphere over L-shell distance. Dashed curves show averages plus/minus the standard deviation, which is a measure of the orbit-to-orbit variability. The lower dashed curve is for most cases below the horizontal axis and not visible. Vertical lines indicate the orbits of moons. Gray shading marks regions of dense rings, which absorb radiation, green shading marks tenuous rings, which can coexist with energetic protons. Regions studied in detail below are marked through yellow areas (Fig. 7). Black curve: Integral intensity I of $\gtrsim 25$ MeV protons measured by the P8 channel of the MIMI/LEMMS instrument. We assume here that this channel measures > 25 MeV protons from all directions with a geometry factor of $\langle G \rangle = 0.05$ cm^{2}sr. A proper calibration will be part of Section 3. The permanent proton radiation belts discussed in this paper are at $1.02 \leq L \leq 1.22$ and $2.27 \leq L \leq 4.88$. Measurements at $L \gtrsim 5$ are dominated by galactic cosmic rays (Kotova et al., 2019). Non-zero measurements in the main rings are from transient cosmic ray secondaries (Cooper et al., 2018). Blue curve: Differential intensity j of 42 keV protons measured by MIMI/CHEMS (Krimigis et al., 2004) through triple-coincidence event data (Vandegriff et al., 2018). Zero measurements are artificially shown as symbols on the x-axis. It can be seen that there are no tens of keV protons counted in the radiation belt region. The shown measurements are linear averages of measurements with $50° - 90°$ equatorial pitch angle and $0 - 20°$ latitude. (For interpretation of the references to color in this figure legend, the reader is referred to the web version of this article.)

plasma. These findings made it clear that a local source needs to be responsible to form and sustain the belts. This process is thought to be cosmic ray albedo neutron decay (CRAND) (Cooper et al., 2018; Cooper and Sturner, 2018), as it is also found at the Earth (Singer, 1958; Hess et al., 1959; Goldhagen et al., 2002; Selesnick et al., 2013). During this process, galactic cosmic rays (GCRs), which are mostly protons at >GeV energies (Usoskin et al., 2005) that are energetic enough to avoid deflection by the planetary magnetic field (Sauer, 1980; Kotova et al., 2019), impact a planet's atmosphere or rings. The subsequent nuclear reactions create a variety of secondary particles, including neutrons. Neutrons escape the production site due to their small interaction with the target material and magnetic fields. Even GCR protons impacting hydrogen, the main constituent of Saturn's atmosphere, can yield neutrons (e.g. Glass et al. (1977)). Neutrons decay into protons with energies that can be magnetically trapped and accumulate in the radiation belts.

Slow radial diffusion is able to explain the smooth shape of the belts and why their phase space density is smoothly decreasing toward the edge of the moon and ring absorption regions instead of only dropping where absorption occurs (Cooper, 1983; Kollmann et al., 2013). Ionization of Saturn's exosphere and subsequent cooling of the protons is able to explain the pitch angle distribution of protons in the innermost radiation belt without involving other processes (Kollmann et al., 2018a). Overall, Saturn's proton belts promise to be very well-controlled laboratories, where the limited number of relevant processes makes it relatively straightforward to test theories with little ambiguities that would result from a mixture with other processes.

However, in recent years it became increasingly clear that the quality of the available calibrated data is insufficient and a bottleneck to further progress on understanding the physics of these belts. The most comprehensive currently existing energetic proton data set is from Cassini's MIMI/LEMMS instrument (Krimigis et al., 2004) that orbited Saturn for over a decade. Calibrated measurements have been available since early in the mission (Krimigis et al., 2005) even though detailed calibration values evolved over time (Krupp et al., 2009, 2018b). The traditional calibration has been successful in quantifying measurements outward of Saturn's radiation belts. Measurements inside radiation belts on the other hand face the challenge that particle species or energy are easily misidentified by an instrument when there are enough particles with sufficient energy to reach its detectors by penetrating through the shielding instead of following the expected trajectories through its apertures. Data products (called "channels") and time periods that are dominated by misidentified particles were found by testing the data for self-consistency, for example by studying the responses to energy and species dependent signatures of moon absorption (micro and macrosignatures) and to obscuration by the instrument's calibration shield and spacecraft parts (Roussos et al., 2007, 2011). Such poor quality data was removed from analysis. However, evidence was accumulating that such filtering was not sufficient.

Firstly we found that even when organizing the data with L-shell and equatorial pitch angle that there is a dependence on latitude, which should not be the case according to Liouville's theorem. This dependence is found for all permanent radiation belts, even though it is subtle outside of the main rings (Roussos et al., 2011) and did not appear to be critical. That changed with the discovery of Saturn's innermost radiation belt, where the latitude dependence turned out to be a major parameter to organize the raw data (Roussos et al., 2018b). Another key property of the innermost radiation belt is that its loss cone is larger than the instrument aperture. When the loss cone is resolved, it is possible to immediately identify non-zero measurements in the loss cone as contamination, which is the case in the innermost belt. It was then realized that the apparent latitude dependence was a direct result of the traditional calibration not properly accounting for particles with energies well beyond the original design range of the instrument. Such very energetic particles do not necessarily enter through the instrument apertures but can penetrate the shielding from any direction, which is why pitch angle does not organize the data well. The penetrating particles were most abundant in the equatorial plane, which is why the count rates changed with latitude.

Spectra for the innermost radiation belt were retrieved with an updated calibration and a more complex analysis method than traditionally used (discussed in Sec. 2.2). The spectra were found to be harder than what the traditional calibration was suggesting for the radiation belts outward of the rings (Kollmann et al., 2011, 2013). This

difference was plausible given that the physics of these belts differed (losses mainly to the exosphere, (Kollmann et al., 2018a) vs. mainly due to diffusion to the moons, (Kollmann et al., 2013)). Then new spectra for the CRAND process were published (Cooper et al., 2018; Cooper and Sturner, 2018) that, different to earlier work at Saturn (Cooper, 1983; Blake et al., 1983), now extended to low enough energies to be compared with the measured proton spectra. The new CRAND spectra resembled the innermost belt but not the outer belts, even though all belts are thought to be sourced by CRAND. This was the second indication that the traditional calibration is insufficient for all proton belts.

Even if penetrators are less important at the outer belts, one issue that the traditional calibration is facing is that the available channels respond to very broad energy ranges. Such channels can be used to estimate the average intensity for each respective energy range. However, combining such values does not construct spectra with reliable shapes (Selesnick and Blake, 2000), even though that had been common practice (e.g. Armstrong et al. (2009)), also for similar instruments (e.g. Krimigis and Armstrong (1982)).

Evidently it is time to apply the same calibration and methods to the measurements of the radiation belts outward of the main rings than we did inward of the rings and by this provide a basis for further analysis of the physical processes involved.

2. Data and calibration

2.1. Data set

Cassini's orbit was continuously evolving (Krupp et al., 2009) and not every orbit was sampling the proton belts. The belts between A- and F-ring and Janus were barely covered, which is why we are not considering them here. Saturn's proton belts show a time dependence that is strongest for the outermost belt between Enceladus and Tethys (Kollmann and Roussos et al., 2017), which is why we are also not including this belt.

For the remaining three belts between Saturn and the C-ring, as well as between Janus, Mimas, and Enceladus, we select L-shell ranges near their intensity peaks: $1.060 \leq L \leq 1.065$, $2.62 \leq L \leq 2.68$, and $3.27 \leq L \leq 3.31$. These are highlighted as yellow shading in Fig. 1. Even though at least the latter belt shows some time variation (Kollmann and Roussos et al., 2017), its amplitude is marginal and will turn out to be smaller compared to the uncertainty in the flux levels of the spectra that we will derive. Different times sample different latitudes and pitch angles. In order to not confuse latitude and pitch angle dependence with time dependence, we filter the data outward of the main rings for the periods of 2015–2017. The innermost belt was only sampled during 2017, where we use all available measurements.

We organize these data for the radiation belts outward of the main rings with L-shell and magnetic latitude calculated from a simple offset dipole as we have earlier (Roussos et al., 2011; Kollmann and Roussos et al., 2017).

Such a dipole model is insufficient for the innermost radiation belt. Instead we use a third-order multipole model that we already used earlier (Roussos et al., 2018b; Kollmann et al., 2018a; Roussos et al., 2018c). This model is optimized to trace the magnetic field from Cassini's locations to ring features that leave signatures in the particle data. Such mapping is critical for this analysis and the reason why we are not using models that aim to fit the global field (Dougherty et al., 2018).

We calculate in the chosen field model the radial distance where Cassini's respective field line crosses the magnetic equator. Because the bulk of our analysis will be based on L-shell, we will refer to the equivalent quantity in the innermost belt also as L-shell, even though other names such as M-shell have been used (e.g. Allegrini et al. (2020), Kollmann et al. (2021)). For the innermost belt we also calculate an effective latitude, which is the latitude measured from the magnetic equatorial plane in a dipole field that has the same L-shell and ratio between local and equatorial magnetic field as our third-order multipole model. The effective latitude is by definition identical to the magnetic latitude of a dipole.

Within these L and time ranges, we bin the measurements in latitude and equatorial pitch angle. A set of bins for each belt is shown in Fig. 2. For each belt we will enumerate the bins in pitch angle and latitude of all used channels with a running index i that will be used in the following section.

2.2. Forward model

A "channel" of a particle instrument counts particles within certain ranges of energy, direction, and mass that are detected over a certain time, which yields a count rate R of counts per time interval. Traditional calibration directly inverts R into an intensity j by dividing it with an effective energy range ΔE over which the channel is sensitive and an effective geometry factor $\langle G \rangle$ for this range:

$$j \approx \frac{R}{\langle G \rangle \, \Delta E} \tag{1}$$

Such an approach is only good when the differential geometry factor g_d, which accounts for the energy and direction dependence of the instrument response (Eq. (19)), and j do not change much over ΔE (e.g. Kronberg and Daly (2013)). This is not the case for the channels we use in Saturn's radiation belts, which is why we use a forward modeling technique instead.

Forward modeling, which we will describe below, can be applied in principle to instantaneous measurements that are taken over broad energy ranges as long as the bulk of the particles enter through the nominal aperture of the instrument (Kollmann et al., 2018b). However, processing is much more complex than the traditional calibration, which is why it is not practical to make it a standard technique. With instantaneous measurements it may be possible to identify the species and energy of penetrating particles (e.g. Kollmann et al. (2021)). A full characterization of the particle population, including the pitch angle distribution of the penetrators, however requires to combine measurements at different latitudes (Roussos et al., 2018b; Kollmann et al., 2018a), no matter the analysis technique.

Instead of going directly back from the measured count rate R to j, "forward modeling" goes forward, from an assumed j to a count rate. We assume j, calculate the expected count rate R_f (Eq. (2)), determine the difference Δ (Eq. (3) below) to the measured R, and then optimize the assumed j until Δ reaches a minimum. We also check if the minimum Δ is reasonably small and if the optimal parameters are at the edge of their respectively allowed range. Both tests were useful during development but are no issue for the distributions presented here. We optimize j by parameterizing it with different spectral shapes that we discuss in Section 3. The optimization of the parameters is implemented through the CONSTRAINED_MIN procedure of the software Interactive Data Language (Harris Geospatial Solutions, 2009).

$$R_f^i\left(\langle \alpha \rangle^i, \lambda^i\right) = \int_0^{\pi} \mathrm{d}\theta \int_0^{2\pi} \mathrm{d}\varphi \int_0^{\infty} \mathrm{d}E \; j(E, \alpha, \lambda^i) \; g_d(E, \theta, \varphi) \; \sin(\theta) \tag{2}$$

g_d is the differential geometry factor, sometimes also called response function, which depends on particle species and scales with both energy and incidence direction. Differential geometry factors for several of the used channels are shown in Fig. 3. The figure caption explains different behaviors that a response function can have. Particularly we want to point out the area of the nominal response, which is what the different channels were designed to measure. The nominal response is limited by the size of the aperture and covers a well defined energy range. In contrast to that we have the response to high energy and penetrating particles that can dominate over the nominal response when the environment has enough of these particles. In Appendix A we show how g_d can be derived from Monte Carlo simulations of particles passing an instrument.

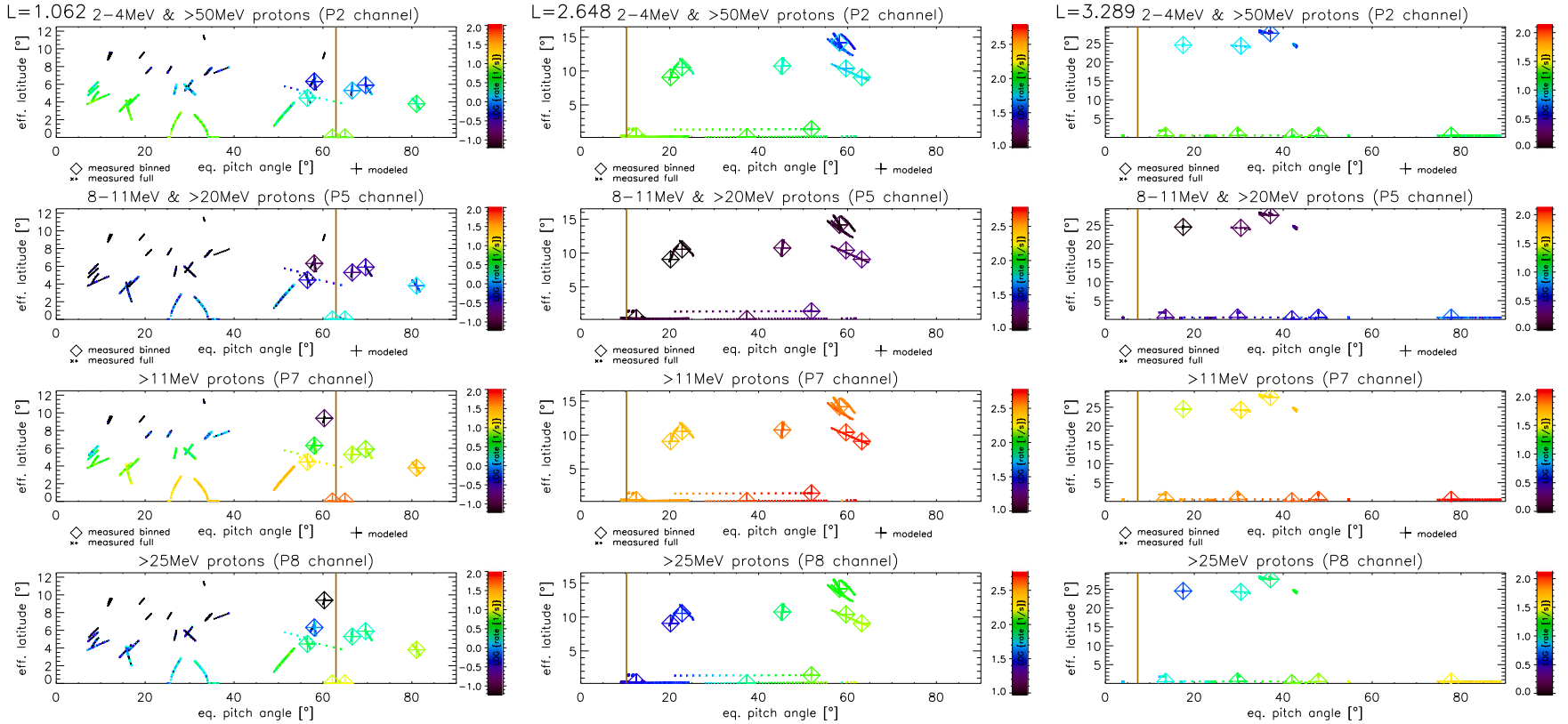

Fig. 2. Count rates at $1.060 \leq L \leq 1.065$ (left column), $2.62 \leq L \leq 2.68$ (middle column), and $3.27 \leq L \leq 3.31$ (right column) as a function of equatorial pitch angle and latitude. Different panels in each column show the measurements by different channels that respond to different energy ranges. We use data throughout 2017 for the left column and data from the beginning of 2015 to the beginning 2017 otherwise. Small symbols show the measurements in native resolution, large diamonds the binned measurements. Large plus symbols show the count rates retrieved from forward modeling using the method from Section 2.2 and the assumed intensity spectral shape from Section 3.5. The brown vertical line indicates the nominal location of the loss cone. (For interpretation of the references to color in this figure legend, the reader is referred to the web version of this article.)

$\langle\alpha\rangle$ is the pitch angle in which the instrument is pointing relative to the magnetic field. α is the equivalent angle in which the particle is moving. For penetrating particles these two angles are unrelated despite their similar names. θ and φ characterize the particle velocity relative to the instrument. The relation between these angles that is needed to evaluate Eq. (2) is provided in Appendix B together with their exact definition.

The indices i enumerate measurements of the used bins at the current L-shell in $\langle\alpha\rangle^i$, λ^i, and channel. (i therefore also runs from channel to channel.) We show an example set of modeled R^i_f and respectively measured R^i values in Fig. 2.

The difference between modeled and measured rate is quantified via the root-mean-square error Δ.

$$\Delta = \sqrt{\sum_i^I (\delta_i)^2} \Big/ I \tag{3}$$

with $\delta_i = \log R^i - \log R^i_f$, where i runs over all I bins at the current L-shell. In our case I is between 28 and 36, depending on the pitch angle and latitude coverage of the respective radiation belt.

3. Physical and phenomenological models

Using a forward modeling technique (Section 2.2) to calibrate the data relies on assuming a functional shape in energy and pitch angles. In this section we discuss different shapes. We start out with flexible functions that are found to phenomenologically fit the raw measurements well (Section 3.1–3.3). Then, instead of adding more free parameters, we calculate shapes that are expected based on some simple physical models that we then directly feed into the forward modeling used to calibrate the data (Section 3.4–3.5).

Overall we assume that j can be factorized, meaning that it can be described through a function in energy that does not depend on pitch angle and a function in pitch angle that does not depend on energy:

$$j(\alpha_{eq}, E) = j(E) J(\alpha_{eq}) \tag{4}$$

j are differential intensities and J is a dimensionless quantity.

This assumption is reasonable because the shapes of pitch angle distributions commonly stay similar for wide energy ranges (Roussos et al., 2011; Clark et al., 2014) and because Saturn's CRAND source, when modeling the rings as a slab of material, only shows weak anisotropy (Cooper, 1983). This simplification is useful to get the analysis started. As it yields reasonable fits (as already hinted in Fig. 2 and discussed below), there is no immediate need to relax the assumption at this stage. Further studies of the pitch angle dependence and how it changes with energy may be subject of future refinements.

3.1. Pitch angle distribution

The pitch angle distribution (PAD) of the innermost radiation belt with its enormous loss cone has been successfully described through a physical model based on interaction with the exosphere and D-ring (Kollmann et al., 2018a). As we are here mostly interested in the belts outward of the rings where the loss cone is barely resolved, we will use simpler, phenomenological PAD instead.

For the shape J of the PAD we assume a Sine-function to the power of $\widetilde{N}$, which is a common description of PADs (Rymer et al., 2008; Clark et al., 2014) that was already applied earlier to this data (Roussos et al., 2018b; Kollmann et al., 2018a). We found that $\widetilde{N}$ easily varies over two orders of magnitude between radiation belts (Section 4.2), which is why we replace $\widetilde{N}$ with 10^N to make the forward model optimization converge faster. The PAD cuts off at the loss cone angle C. The full expression we use is

$$J(\alpha_{eq}) = \frac{1 + \exp\big((C - \alpha_0)/k_t\big)}{\sin^{10^N} \alpha_0} \frac{\sin^{10^N}(\alpha_{eq})}{1 + \exp\big((C - \alpha_{eq})/k_t\big)} \tag{5}$$

$\alpha_0 = 90°$ is chosen without loss of generality. We use $k_t = 0.18°$ that leads to a steep drop at the loss cone.

The geometric loss cone C is the largest equatorial pitch angle where charged particles reach Saturn's 1-bar surface at latitude λ_s and magnetically mirror from there. It is calculated based on conservation of the first adiabatic invariant during the bounce motion (Roederer, 1970).

$$C = \arcsin \sqrt{\frac{B\big(L, \lambda = 0\big)}{B\big(L, \lambda = \lambda_s\big)}} \tag{6}$$

B is the magnetic field. The exact value is not critical outside of the main rings because the loss cone is much narrower than the LEMMS apertures. We assume in this region a dipole field where $\lambda_s = \arccos\sqrt{1/L}$. Inward of the rings we calculate λ_s through tracing in our magnetic field model to the poles.

Example curves for the shape of the assumed pitch angle distribution will be shown together with the final results in the right panel of Fig. 7.

3.2. Power law model

Given that energetic particle spectra commonly form power-law-like spectra we initially assume such a shape:

$$j = \frac{10^{j0}}{1 + \exp\big((E - 10^{Ec})/E_s\big)} \left(\frac{E}{E_0}\right)^{\gamma} \tag{7}$$

The power law exponent is γ. The overall amplitude of the function is optimized through changing the parameter j_0 that relates to the logarithm of the intensity at a reference energy that we chose as $E_0 = 38550$ keV.

We know that a magnetic field is only able to trap particles up to a certain energy. We therefore cut the spectrum off at energy $\widetilde{E}_c = 10^{Ec}$. The steepness of the cutoff is fixed to $E_s = 10^4$ keV.

We estimate the cutoff energy at Saturn through the following analytic expression (Appendix C):

$$\widetilde{E}_c = \sqrt{(m\,c^2)^2 + \left(c\,\eta \frac{q B_s R_s}{3L^2}\right)^2} - (m\,c^2) \tag{8}$$

m is the proton rest mass, c the speed of light, $\eta = 1/8$ (Thomas and Doherty, 1971; Cooper et al., 2018), q the charge of the particle, B_s and R_s Saturn's equatorial surface magnetic field and radius, respectively. Numerical particle tracing discussed in Section 3.3.3 will show that this value should be considered as an upper limit. While we initially consider a fixed value of $\widetilde{E}_c$ we treat it as a free parameter in Section 3.3.3.

3.2.1. Channel selection

After selecting the assumed functional shape, we need to decide on a set of measurement channels to base the analysis on. Naively one could simply use all available channels but there are several reasons against this. Firstly, several channels that were designed to measure protons also measure other species such as electrons. As we do not want to solve simultaneously for an electron distribution at this stage, we need to exclude such channels. The electron issue is discussed more below in this section.

Secondly, there are channels that in the radiation belts respond mostly to penetrating particles. Because such channels often share a similar penetrator response, considering too many of such channels may bias the spectrum to fit mostly penetrator energies instead of the full energy range. The bias issue is discussed more in Section 3.3.1.

We will use three sets of channels throughout this paper.

- Set 1: A5, A6, A7, P2, P3, P5, P6, P7, P8
- Set 2: P2, P5, P7, P8
- Set 3: P2, P5, P7, P8, E7

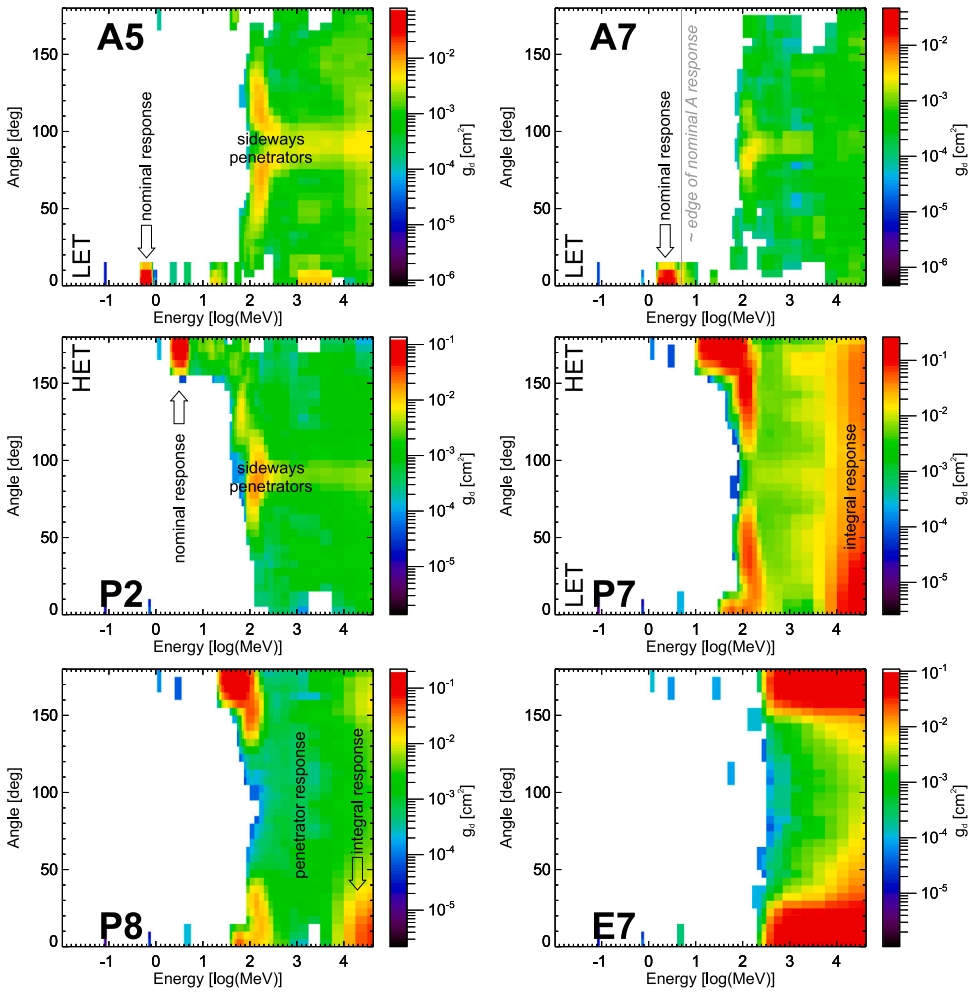

Fig. 3. Differential geometry factor for the detection of protons for several LEMMS channels used in our analysis as a function of energy and incidence angle θ. Angles $\lesssim 7.5°$ refer to incidence into the low energy telescope (LET), angles $\gtrsim 165°$ to incidence through the wider high energy telescope (HET). Penetrating particles may enter through any other direction. "A" channels (such as the shown A5 and A7 channels) respond to $\lesssim 10^{0.7}$ MeV protons within a narrow energy range that enter through the LET. "P" channels respond to protons entering through the HET over a wider energy range. When a response starts at some energy but does not have an upper bound, is referred to as an integral response. The A channels and P2 have a strong response to sideways penetrators entering from angles around 90°, while most other channels typically show a more omnidirectional response to penetrators. Numerical values are provided in the online Supplementary Material. (For interpretation of the references to color in this figure legend, the reader is referred to the web version of this article.)

"A" channels that are included in set 1 are based on coincidence or anti-coincidence measurements by 2 detectors in LEMMS' low energy telescope (LET). The A channels used here nominally cover the proton energy range from 510 keV to 4.0 MeV but also respond to $\gtrsim 100$ MeV (Fig. 3). In contrast, the "P" and "E" channels are based on up to 4 detectors in the high energy telescope (HET) with up to three detectors for positive coincidence (Krimigis et al., 2004). The P channels used here nominally respond to 2.3 MeV to 39 MeV protons, and E7 nominally responds to 7 to 20 MeV electrons. These channels also respond to $\gtrsim 100$ MeV protons (Fig. 3).

Set 1 is what we used earlier to determine proton belt spectra (middle panel in Fig. 4, Kollmann et al. (2013)). These channels were selected because their net response to electrons was found to be negligible (Roussos et al., 2011). "Net" response means that while some of the used channels have in principle a sensitivity to electrons, that the electron count rate contribution is insignificant compared to the proton count rate. The electron contribution can be tested by checking the radial distributions of channels throughout the radiation belts. $\lesssim 6$ MeV electrons are unaffected by absorption through the moons and the G-ring (Kollmann et al., 2011). Channels with significant intensities in the respective absorption regions therefore have to respond to electrons. This is not the case for the used set of channels, which show deep separations between the proton belts, as illustrated for few of these channels in Fig. 1, Armstrong et al. (2009), and Kollmann et al. (2013) and discussed for the full set in Roussos et al. (2011).

The best fitting spectrum when using set 1 is shown in the left panel of Fig. 4. It has a slope of $\gamma = -0.3$, which is unusually hard, and an average difference for each bin of data and model of $\Delta \approx 0.02$.

The high number of coincidences in the "P" channels means that these channels are more likely to properly identify a particle, different to the "A" channels. This is why we introduced set 2 that only uses "P" channels. As another improvement, set 2 only uses channels with notable anisotropies, which are an indication (though not proof) that a measurement has a contribution from particles that enter through the aperture, as the instrument design expected. The best fit based on set 2 is also shown in the left panel of Fig. 4 and has a slope of $\gamma = -0.8$, which is steeper and harder, and has an average error of $\Delta \approx 0.01$, which is about half of set 1.

The different sets of channels are sensitive to different energy ranges. The larger error of the larger set of channels therefore may be an artifact of trying to fit a larger energy range with the same power law. We investigate this in the next section.

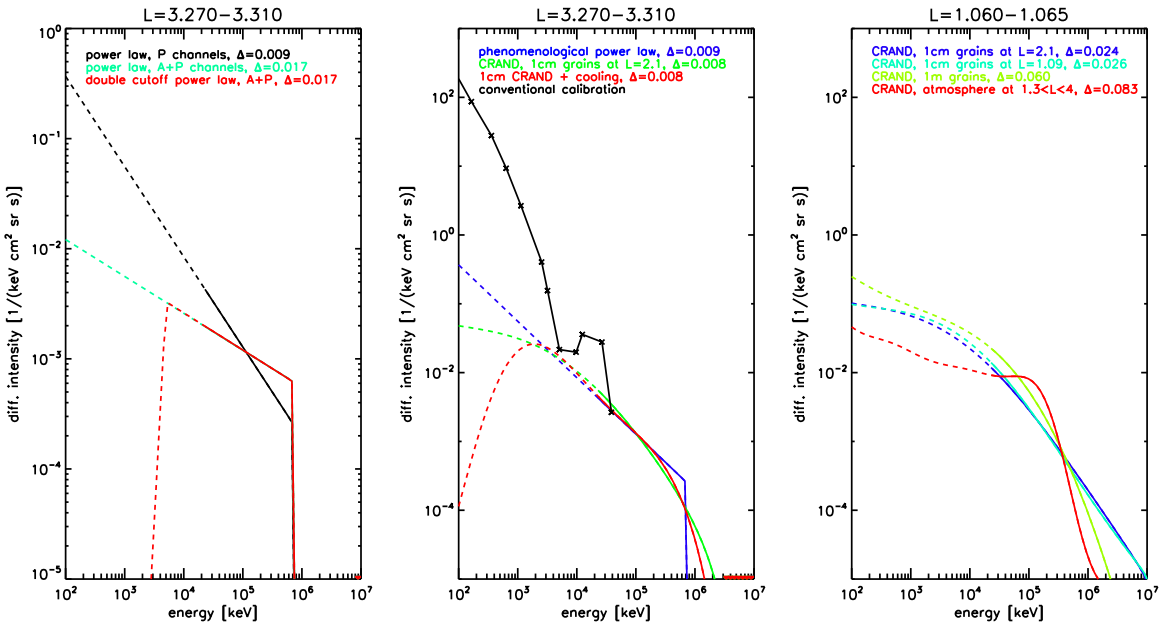

Fig. 4. Compilation of different considered proton spectra for the belts located between Mimas and Enceladus (left and middle panels) and the belt inward of the main rings (right panel). The best spectra will be presented in Fig. 7. Solid curves mark the energy range that is constrained by the measurements (see Section 3.3.2), the dashed curves are assumed shapes that cannot be constrained. Left panel: Different results when using sets 1 and 2 of measurement channels (black vs. green, Section 3.2.1) and when assuming different spectral shapes (green vs. red). The smallest error Δ is found for using channel set 2. Comparing the red and green curves and their respective errors shows that the measurements are not sensitive to the low energies nominally measured by the A channels. Middle panel: Different spectral shapes (discussed in Section 3.2–3.5) used in the forward model using channel set 2 (blue, green, red). We compare with results from the traditional calibration (black, Kollmann et al. (2013)). Traditional and new calibration only agree at $\approx$ 40 MeV. Right panel: Different spectral shapes (discussed in Section 3.4) using channel set 3. The smallest error is found for CRAND mostly occurring in 1 cm ring grains. (For interpretation of the references to color in this figure legend, the reader is referred to the web version of this article.)

3.3. Double cutoff power law

We now construct a function that follows a power law with exponent γ_1 below energy E_K and a power law with exponent γ_2 above. Like before, we cut off the spectrum at 10^{Ec}.

$$j = \frac{10^{j0}}{1+\exp\left((E-10^{Ec})/E_s\right)} \left(\frac{E_K}{E_0}\right)^{\gamma_2} \left(\frac{E}{E_K}\right)^{\gamma_1} \text{for } E \le E_K \quad (9)$$

$$j = \frac{10^{j0}}{1+\exp\left((E-10^{Ec})/E_s\right)} \left(\frac{E}{E_0}\right)^{\gamma_2} \text{for } E > E_K \quad (10)$$

3.3.1. Channel selection, continued

We set $\gamma_1 = +10$ so that E_K effectively becomes a low energy cutoff. We set $\gamma_2 = -0.3$, which is the optimum value determined for the A channels (Section 3.2), and set the lower cutoff to $E_K = 10^{3.7}$ keV, which is just above the nominal energy range of the A channels (highlighted in the upper right panel of Fig. 3). Assuming such a spectrum, which does not include particles within the nominal energy range of the A channels, does fit the measurements of set 1 as well as assuming a power law that continues to lower energies. The respective spectra and their errors are illustrated in left panel of Fig. 4.

The A channels therefore do not constrain the lower energies, which would be the main reason to include them in the analysis. Their nominal, low-energy response does not provide significant count rates. Instead, their count rates are dominated by penetrators. This can be understood qualitatively by comparing in Fig. 3 the small red area at low energies for the nominal response with the large green and orange areas at high energies for the penetrator response. If there are enough particles at high energies, which is the case in the proton belts, the largest response area dominates the count rates.

The discrepancy in optimal spectra when including channels that are dominated by penetrators suggests that our instrument response to penetrators is not entirely accurate, which is not unexpected because details of the instrument shielding are nowadays difficult to reconstruct with certainty (Appendix A).

In the following, we will therefore not use set 1 anymore. Instead, we will only use sets 2 or 3 that only include channels with a significant anisotropy, which suggests that they are not dominated by penetrating particles. (We will later find that even some anisotropic channels such as "P2" are still dominated by penetrators, see Section 4.2. This is acceptable because we are able to reproduce this response.) For the same reason, we chose to exclude measurements of the innermost radiation belt that are deep in the loss cone, which are dominated by penetrators.

The difference between sets 2 and 3 is the inclusion of channel E7. This channel was designed to measure energetic electrons and therefore cannot be used outward of the main rings, where MeV electron intensities are high. However, channel E7 also does respond to protons, a fact that we confirmed in Earth's inner radiation belt (Roussos et al., 2018b). Inward of Saturn's main rings we did not find notable electron intensities (Roussos et al., 2018b) so that we can make use of the proton response of this channel. Adding E7 is beneficial because it allows to identify spectral features around 300 MeV, where it starts responding to protons (Fig. 3).

3.3.2. Constrainable energy range

After finding that the nominal energy range of the involved channels is unrelated to the energy range that we are able to constrain within the radiation belts, we systematically check what the constrainable energy range is. To do this, we gradually change the values of the lower cutoff E_K, while otherwise maintaining the spectral shape. It can be seen in the left panel of Fig. 5 that the error Δ is rising when E_K cuts into the spectrum beyond $E \gtrsim 20$ MeV. That means that our measurements are not sensitive below 20 MeV.

3.3.3. Protons have up to $\approx$ 1 GeV energies

Fig. 3 shows that we have channels available that change their response at energies as high as $\approx$ 10 GeV, which means that we may resolve spectra roughly until this energy.

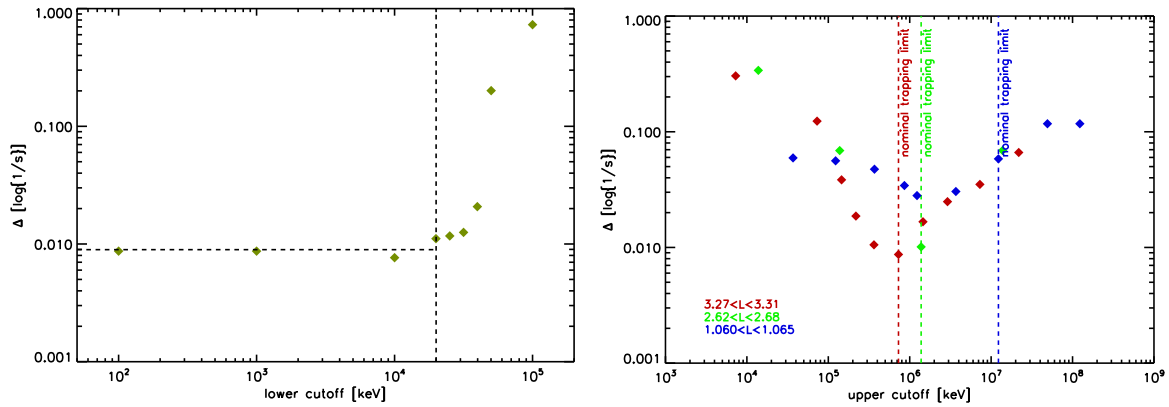

Fig. 5. Left panel: Investigation over which energy range the available measurements are sensitive to (see Section 3.3.2). We assume a spectrum (Section 3.3), change the lower cutoff energy (x-axis), and observe the data-model discrepancy Δ (y axis). It can be seen that the presence of $\gtrsim 20$ MeV intensities does make a difference for the modeled count rates, showing that the measured count rates are sensitive to $\gtrsim 20$ MeV. Right panel: Effect of the upper energy cutoff on Δ (see Section 3.3.3). It can be seen that the best fit for all radiation belts (different colors) is at 1-2GeV. Vertical lines are estimates of the trapping limit, which is an upper limit (Section 3.3.3). (For interpretation of the references to color in this figure legend, the reader is referred to the web version of this article.)

We now change the assumed upper cutoff energy E_c systematically. Outward of the rings, we use channel set 2. Inward of the rings we can use set 3 and do so. Results are shown in the right panel of Fig. 5. Different to Section 3.3.2, where Δ did not change below a threshold, here we find a clear minimum at $\approx 1-2$ GeV. A minimum indicates that we are able to find a spectral structure, namely the cutoff, at the respective energy.

For the belts outward of the main rings (red and green curves) the determined cutoff is close to what is expected for the trapping limit (see Eq. (10)). For the innermost belt it is an order of magnitude below.

Besides the trapping limit that we determine through the magnetic field gradient (Appendix C), we need to consider if the particles can gyrate without hitting the planet. The gyroradius of a 1GeV proton at $L = 1.06$ is $r_g = 0.005 R_S$, which is an order of magnitude lower than the equatorial distance to the planet. This means that the gyroradius is not able to explain the relatively low cutoff in the innermost belt.

In order to confirm the analytic estimates of the trapping limit in the inner belt we numerically traced particles in an offset dipole field. The tracing uses a modified leapfrog technique (Vay, 2008) that we already used before (Kotova et al., 2019) and that works best for relativistic particles moving on large scales, as is the case here. Results are shown in Fig. 6 and support that 1GeV proton can gyrate between planet and the main rings. $\gtrsim 5$ GeV protons, on the other hand, are not able to maintain a stable gyro and bounce motion around the planet, since their gyroradius in this region is comparable with the curvature of the magnetic field lines they suppose to follow.

We therefore conclude that our analytic calculation of the trapping limit only provided an upper limit and that the actual value is around 5GeV. The inferred cutoff is with a few GeV at slightly lower energies, a discrepancy that is insignificant given the broad energy response of the measurement channels we are using. Based on the similarity of the measured and predicted cutoff, we conclude that it likely results from the magnetic field geometry, not any other loss process.

3.4. CRAND source

While cutoff power laws fit the data reasonably well, they do not provide immediate understanding on the source and loss processes that cause such a spectrum. In the following sections, we will therefore use spectral shapes that are based on physical theories. The amplitude of the spectra will remain a free parameter that we determine based on the measurements.

To date, the best explanation for the existence of proton belts inward of the moon and ring orbits is that they are locally produced by CRAND (Section 1, Roussos and Kollmann (2021)). During the CRAND process, galactic cosmic rays impact Saturn's main rings and/or the atmosphere, and create secondary neutrons, some of which decay back into protons and sustain the radiation belts.

We calculated CRAND spectra earlier (Cooper et al., 2018; Cooper and Sturner, 2018), Appendix D and now use the spectral shapes as input to our forward model. CRAND spectra differ, depending if the neutrons are produced in the atmosphere or the rings, and depending on the grain size within the rings. The available CRAND spectra are hardest and softest when assuming that the rings consist only of 1 cm or 1 m grains, respectively.

The used CRAND models (Cooper et al., 2018) represent the rings as optically thin collections of spherical grains of a certain size, similar as it has been done earlier (Blake et al., 1983). It is therefore grain size that scales our CRAND spectra, not ring density.

Depending on location, Saturn's magnetic field only lets cosmic rays above a certain energy enter. We chose cosmic rays that are able to reach $L = 2.1$ (region of the A ring) and $L = 1.09$ (the inner edge of the D ring). Similarly we chose cosmic rays impacting the atmosphere at latitudes that trace to $1.3 < L < 4$. The right panel in Fig. 4 shows the respective spectra as well as the error Δ. It can be seen that the best fits are found when assuming emission from 1 cm grains in the A ring.

The small value of Δ when reproducing the measurements when assuming CRAND-shaped spectra provides further support that CRAND is the dominating source process. The importance of CRAND has been suggested for a long time (Section 1) based on spectra that we now know were unreliable. This was possible because the earlier conclusion was based on the radial distribution of the proton belt phase space density (Kollmann et al., 2013) that suggested a local source.

3.5. Proton cooling

In Section 3.4 we assumed that the radiation belt spectrum is identical to the CRAND source spectrum. Generally, CRAND cannot be the only process acting in the proton belts, otherwise their intensity would accumulate until infinity. The main process that balances the source outside of the main rings is thought to be radial diffusion to the moon orbits, where the protons are absorbed (Cooper, 1983; Kollmann et al., 2013; Kollmann and Roussos et al., 2017). If this diffusion is energy independent, it will not change the spectral shape and therefore be irrelevant for our purposes. Generally, radial diffusion can be energy dependent based on what exactly is driving it. Such dependence typically relates on how the power spectrum of field fluctuations changes with the particle drift frequency (Lejosne and Kollmann, 2020). However, previous radiation belt modeling did not require to introduce a notable energy dependence in the diffusion coefficient (Kollmann et al.,

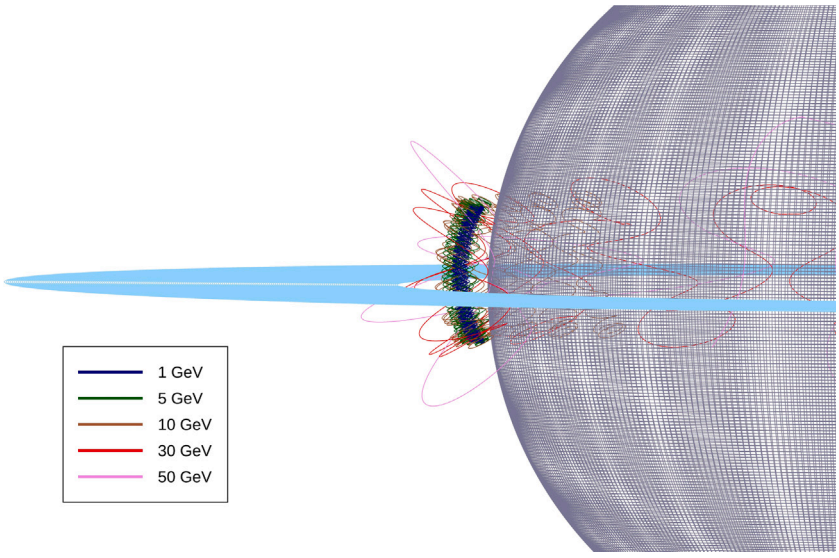

Fig. 6. Trajectories of very high energy protons in Saturn's magnetic field.

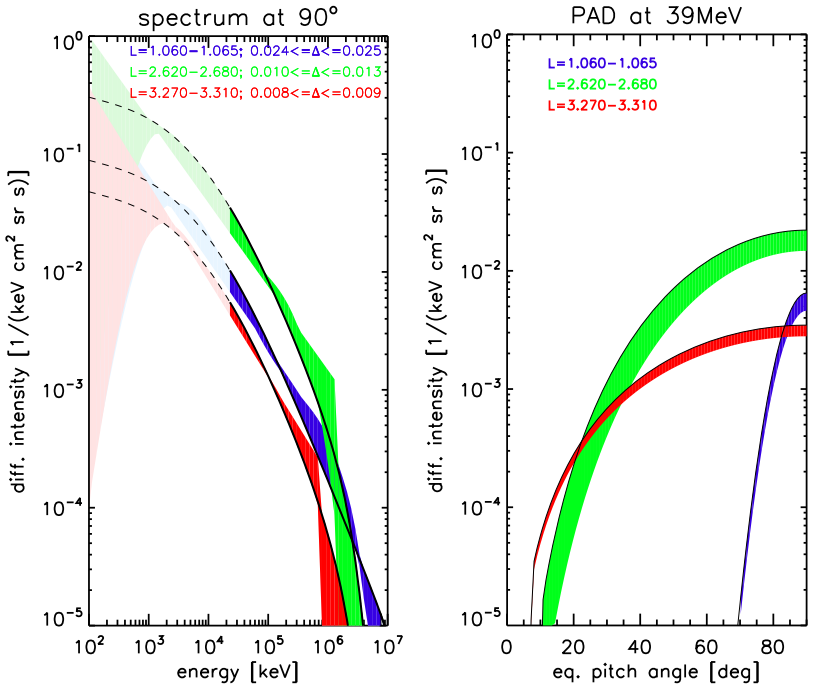

Fig. 7. Best fits for the three proton belts considered here: between Saturn and the D-ring (blue), Janus and Mimas (green), Mimas and Enceladus (red). All shown forward model results (Eq. (2)) can be considered to be consistent with raw measurements from channel set 2. Data-model discrepancies can only be shown as count rates (as in Fig. 2). We represent them here through the values of Δ given in the labels. The underlying models assume different spectral shapes: Black curves are spectra assuming a spectral shape identical to the CRAND source (Section 3.4). The envelopes arise from also assuming either a power law shape or CRAND plus cooling. Left: energy spectra at pitch angle 90°. Other pitch angles show by definition a different overall intensity but the same spectral shape. Right: Pitch angle distributions at 39 MeV. Other energies show a different overall intensity but the same shape in pitch angle. The measurements only constrain the spectra shown as solid curves and strong colors. Numerical values are provided in the online Supplementary Material. (For interpretation of the references to color in this figure legend, the reader is referred to the web version of this article.)

2013). Otherwise determined diffusion coefficients scatter by orders of magnitude (e.g. Van Allen (1984)) and there exist currently no strong constraints on the energy dependence of the proton coefficients.

Therefore we consider another process to balance the source that changes the spectral shape in a well-constrained way. This process is cooling, sometimes also called energy loss or energy friction. Protons passing material gradually lose energy, which shifts their spectrum to lower energies until they are eventually absorbed. Materials that may play a role for the proton belts include Saturn's hydrogen corona (Kollmann et al., 2017) and plume (Shemansky et al., 2009), and/or the outskirts of the Enceladus neutral gas torus. Particularly the hydrogen component of the torus is difficult to constrain through numerical models that are used to interpret the available remote and in-situ data (Jurac and Richardson, 2005; Fleshman et al., 2012; Dialynas et al., 2013).

The evolution of the proton phase space density f is described through a differential equation for $\partial f/\partial t$. The contribution $\partial f/\partial t|_E$ of cooling is (Schulz and Lanzerotti, 1974; Kollmann et al., 2013)

$$\left.\frac{\partial f}{\partial t}\right|_E = -\frac{v}{p^2}\frac{\partial}{\partial E}\left(p^2 f \frac{dE}{dx}\right) \tag{11}$$

dE/dx is the differential energy loss per distance in material. v is the proton speed and p its momentum.

CRAND contributes as another term to $\partial f/\partial t$:

$$\left.\frac{\partial f}{\partial t}\right|_S = s_0 s(E) \tag{12}$$

Here we split CRAND into an amplitude s_0 and a functional shape $s(E)$.

Now we assume a steady state, which is a very good approximation for Saturn's protons belts (Kollmann and Roussos et al., 2017). We further assume that the gains through CRAND (Eq. (12)) exactly equal the losses through cooling (Eq. (11)). This is a good approximation for the innermost radiation belt, where cooling is thought to be the dominant loss process. For the outer belts, this assumption will provide a lower limit for the intensities. We also define $f = F_0\, F(E)$. Energy loss dE/dx in material of density ρ is often tabulated as values ϵ that are normalized to a reference mass density ρ_0, so we write $dE/dx = \epsilon\rho/\rho_0$. With all this we get for $F(E)$:

$$0 = -\frac{v}{p^2}\frac{\partial}{\partial E}\left(p^2 \frac{\rho F_0}{s_0} F(E)\frac{\epsilon(E)}{\rho_0}\right) + s(E) \tag{13}$$

It is apparent from Eq. (13) that the ratio of the material density ρ to the amplitude of the CRAND source s_0 is scaling the amplitude F_0 of the proton phase space density but not the shape $F(E)$.

In our forward modeling approach, we assume a value of ρ/s_0, solve numerically for $F_0 F(E)$ as described in Appendix E, calculate the expected count rates, and then iterate on the assumption of ρ/s_0. In principle, the forward modeling method is the same as used before, just that now we are not using analytical functions to describe the spectral shape but a numerical solution of a differential equation.

Results are included in Fig. 4. It can be seen that energy friction modifies the spectrum mostly in the $<$ MeV energy range, which our measurements are not able to constrain.

Overall we find that the CRAND process alone is providing a sufficient explanation for the spectral shape from $\approx$ 20 MeV, the lowest energy we can constrain with LEMMS, to $\approx$ 1 GeV. The overall amplitude of the spectra is likely determined by radial diffusion for the outer belts and cooling for the innermost belt (Section 1). Besides these processes we currently have no indication for the importance of other processes relevant in this energy range.

4. Proton belts compared

4.1. Energy spectra

We now calculate spectra for Saturn's three considered radiation belts. To ensure that the results are comparable we use channel set 2 for all belts even though for the innermost belt we could use set 3. The results are shown in Fig. 7, where it can be seen that the spectra of all belts are approximately similar over the constrainable energy range even when assuming different functional forms such as a power law, the CRAND shape, or CRAND plus cooling.

That similarity may also apply to the permanent proton belts we did not studied here (Section 2.1). More sophisticated filtering and binning of the respective measurements together with an otherwise similar analysis as done here will be required to constrain differences.

All reasonable spectra determined here can be approximated through a power law with exponent $\gamma \approx -1$. The newly determined spectra are therefore much harder/flatter than what was published earlier. Earlier analysis based on a very similar data set of the Cassini/LEMMS instrument that we use here showed an exponent of $\gamma \approx -2$ (black curve in middle panel of Fig. 4, Kollmann et al. (2013)). Measurements by the similar Voyager/LECP instrument (Krimigis et al., 1977) suggested an even softer spectrum with $\gamma \approx -4$ (Krimigis and Armstrong, 1982).

4.2. Pitch angle distributions

Besides the energy spectra, Fig. 7 also shows the respective pitch angle distributions in the right panel.

It can seen that all radiation belts are equatorially trapped for all energies. This fact may be surprising given that we include measurements from channels such as P2, where count rates suggest a field aligned distribution (shown as color coding in the upper panels of Fig. 2 and as line plots in Roussos et al. (2011)). The reason for this behavior is counter-intuitively not the actual pitch angle distribution but an artifact from the instrument response: Several channels are especially sensitive to high-energy protons when they enter perpendicular to the pointing direction of the instrument (see "sideways penetrators" in Fig. 3). Penetrators with $\alpha = 90°$ lead to the highest count rates of these channels when the instrument points into $\langle\alpha\rangle = 0$. We note that while anisotropic measurements may suggest that penetrators are likely not playing a major role for that measurement, that this can sometimes be wrong, as demonstrated by channels such as P2.

Fig. 7 shows that the closer the radiation belt is to Saturn and the larger the loss cone becomes, the steeper the distributions become even outside of the loss cone. Without a physical model of the pitch angle distributions we cannot tell if these shapes are a result of cooling and absorption in the atmosphere, the CRAND injection process, or pitch angle diffusion.

4.3. Comparison with Earth and Jupiter

The discrepancy between earlier spectra of Saturn's proton belts and what we find here is reminiscent on how the understanding of the Earth's inner radiation belt evolved. This belt was the first discovery of the space age (Van Allen and Frank, 1959) but the supposed presence of MeV electrons in this region (e.g. Lyons and Thorne (1973), Johnston et al. (2015)) was never understood (e.g. Kim and Shprits (2012)). Only recent studies showed that most of the detected MeV electrons were actually misidentified MeV protons (Li et al., 2015; Fennell et al., 2015). Also at Saturn it was MeV protons that contaminated the measurements but in this case they were mostly misidentified as hundreds of keV protons.

A comparison of proton spectra from Saturn, Jupiter, and the Earth is shown in Fig. 8. There is no single spectrum that can represent one planet. We chose spectra with high intensities at the highest available energies. For Saturn we picked the spectrum at $L = 2.7$ that we determined here and has the highest intensity from the belts studied in this work.

Earth's spectrum (Selesnick et al., 2017) is taken at $L = 1.4$, which is about the distance where the proton intensities in the hundreds of MeV range peak (Selesnick and Albert, 2019). (If we would search for high intensities in the MeV or tens of MeV range, we would pick spectra near $L = 2$ or $L = 3$, respectively (Johnston et al., 2015).)

At Jupiter there are little reliable proton data for $L < 6$ near the equatorial plane (e.g. Kollmann et al. (2020)). We select a spectrum at $L = 9$ (Kollmann et al., 2021), which is at least near a local intensity peak (Kollmann et al., 2017). There are currently no directly measured proton intensities beyond 30 MeV available at Jupiter (e.g. Nénon et al. (2018)). Physical models (Nénon et al., 2018) and measurements of heavier ions with significant intensities until at least 10MeV/nuc (Roussos et al., 2020a; Kollmann et al., 2021) suggest that proton spectra reach to higher energies, but this is not known to date.

Our comparison shows that $>$ 10 MeV intensities at the Earth are more similar to Saturn than to Jupiter. This is expected because both Earth and Saturn form their proton belts through CRAND.

Intensities at the Earth are an order of magnitude higher than Saturn in the tens of MeV range. This may be related to the fact that Earth's inner belt is also populated through solar protons, solar proton albedo neutron decay, and radial diffusion from the magnetosphere (e.g. Selesnick et al. (2007)), all processes that are unimportant at Saturn.

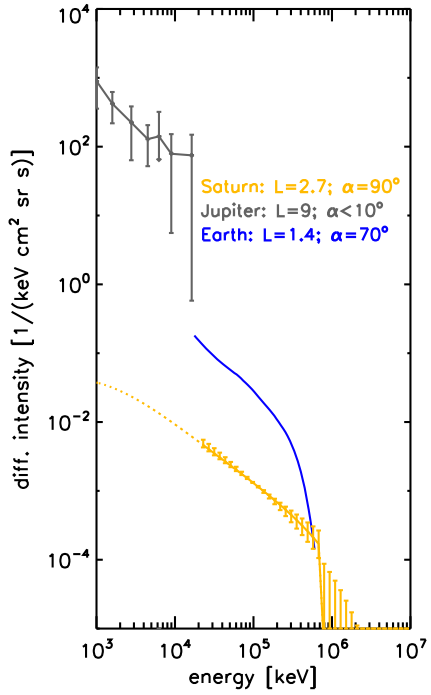

Fig. 8. Comparison of proton intensities at different planets. Orange: Saturn's proton belt between Janus and Mimas at $2.62 \leq L \leq 2.68$ and $\alpha = 90°$, as shown in Fig. 7. Error bars represent uncertainty of the forward model. Gray: Jupiter's proton belt between Io and Europa at $8 \leq L \leq 10$ and $\alpha < 10°$ measured at high latitudes by Juno/JEDI (Kollmann et al., 2021). Error bars represent the time variability. Blue: Earth's inner proton belt at $L = 1.5$ and $\alpha = 70°$ in 2015 measured by Van Allen Probes/REPT (Selesnick et al., 2017). (For interpretation of the references to color in this figure legend, the reader is referred to the web version of this article.)

Earth's spectrum changes slope and begins to cut off around 0.1GeV while Saturn's spectrum only rolls over at about 1GeV, a difference that can be attributed to the difference in local magnetic fields.

The intensities at Jupiter around 10 MeV appear to be several orders of magnitude larger than for Earth and Saturn. (4 orders compared to the shown Saturn spectrum, 1 order when comparing with an Earth spectrum at $L = 1.9$, (Selesnick et al., 2017).) The difference between Saturn and Jupiter is not surprising given that Jupiter does not have to rely on CRAND to produce its ion belts (e.g. Roussos and Kollmann (2021)).

The difference between Jupiter and Earth is more difficult to explain. Even though Jupiter is known for its strong internal plasma sources that are driven by geologically active moons, the maximum plasma densities throughout the magnetospheres of Earth and Jupiter are not that different (Bagenal et al., 2016; Zhelavskaya et al., 2021). Also, intensities at the Earth dominate over Jupiter at and below MeV energies (Mauk, 2014). A difference in the reservoir of particles that can be accelerated therefore cannot be the explanation. The difference therefore likely lies in the acceleration and loss processes. Jupiter's giant magnetosphere easily accelerates particles: Even when only relying on adiabatic transport (e.g. Roussos and Kollmann (2021)) from the dayside magnetopause to the planet, it can increase energies by 4 orders of magnitude (Becker et al., 2021). Also, Jupiter's radiation intensities are relatively stable and vary by only an order of magnitude at $L \lesssim 10$ (e.g. Kollmann et al. (2020)). Earth on the other hand occasionally almost loses its radiation belts at $L \gtrsim 2$ and intensities drop by several orders of magnitude (e.g. Selesnick et al. (2010), Reeves et al. (2016)), which interrupts a potential accumulation to Jupiter-like intensities.

Only very few works have investigated how properties of a planetary system scale its radiation belts. A detailed discussion or quantitative analysis is outside the scope of this paper but warrants further investigation.

5. Summary

Proton intensities in Saturn's radiation belts have been highly uncertain. We use measurements by the MIMI/LEMMS instrument of Cassini that were originally intended to characterize protons in the hundreds of keV to tens of MeV energy range but that in Saturn's proton belts are dominated by penetrating radiation of higher energies. We use detailed knowledge of the instrument response function and a forward modeling technique, where appropriate combined with numerical modeling results, to retrieve proton distributions beyond 20 MeV in 3 of Saturn's proton belts that are peaking between 1 and $4R_S$. Our findings are:

- Saturn has significant proton intensities until 1 GeV (Fig. 5), which is about the energy until which protons near Saturn can be stably trapped (Fig. 6).
- The newly retrieved proton spectra can be approximated as power laws of intensity over energy with exponents of ≈ -1. All studied belts show similar shapes (Fig. 7). Earlier studies suggested softer spectra with exponents $\lesssim -2$.
- Pitch angle distributions become steeper closer to Saturn (Fig. 7).
- We find further support that Saturn's proton belts are sourced through the CRAND process. While the overall amplitude of the radiation belt spectra is likely determined by radial diffusion (outward of the rings) or cooling (inward) we did not find evidence of additional processes affecting the spectral shape in the 20 MeV to 1 GeV range.
- Saturn's proton intensities in the tens of MeV energy range are weaker than at Earth and Jupiter (Fig. 8), possibly because these other belts are not solely sourced by CRAND.

Acknowledgments

The authors like to thank T. P. Armstrong (FTECS) for useful discussions on the LEMMS response, Andreas Lagg (MPS) and Jon Vandegriff (JHU/APL) for extensive software support, and Martha Kusterer (JHU/APL) for reducing the MIMI data. The work at JHU/APL and NASA/GSFC was funded through NASA's Cassini Data Analysis Program (CDAP), grant 80NSSC20K0478. Earlier the JHU/APL authors were partially supported by the NASA Office of Space Science under task order 003 of contract NAS5-97271 between NASA/GSFC and JHU. The MPS authors as well as the German contribution of the MIMI/LEMMS Instrument were in part financed by the German BMWi through the German Space Agency DLR under contracts 50 OH 0103, 50 OH 0801, 50 OH 0802, 50 OH 1101, 50 OH 1502 and by the Max Planck Society. The Cassini/MIMI data and a user guide are available online through NASA's planetary data system (PDS — https://pds.nasa.gov/).

Appendix A. Calibration accounting for penetrators

In this section we describe the simulations of the LEMMS geometry factors that are used in the forward model discussed in Section 2.2.

A.1. LEMMS model

We constructed a 3D-model of LEMMS using the Geometry Description Markup Language (GDML) based on hard copies of mechanical drawings of the instrument. Because no digital Computer Aided Design (CAD) model of the instrument could be retrieved for direct conversion into GDML, all elements of LEMMS were created using basic volumes of mostly cylindrical, rectangular and hexagonal shapes, as well as their boolean intersections and/or subtractions. Inspection of a structural model of LEMMS was also an important part of the model design process. This procedure came with uncertainties: the mass of our GDML model is only 95% of the actual mass of LEMMS (6.72 kg). Additional details of the modeling procedure are provided in Roussos et al. (2018b).

The spacecraft was not included in the model.

An improvement of the LEMMS model used here compared to the earlier version from Roussos et al. (2018b) is that we have also introduced the static magnetic field generated by permanent magnets on LEMMS's LET side. After setting up the geometry, we then simulate the LEMMS response to energetic charged particles using the GEANT4 Radiation Analysis for Space (GRAS) software (Agostinelli et al., 2003; Santin et al., 2005).

A.2. From GEANT results to response functions

This section elaborates on how the output of these simulations is used to calculate the differential geometry factors shown in Fig. 3 and Roussos et al. (2018b).

First we calculate the intensity j_0 used in our simulation from the number of simulated particles. The differential intensity j_0 is the number $\mathrm{d}N_i$ of protons per area $\mathrm{d}A$, solid angle $\mathrm{d}\Omega$, energy interval $\mathrm{d}E$, and time $\mathrm{d}T$. We inject protons from a spherical surface of radius r = 17 cm surrounding the instrument. The injected intensity is isotropic and therefore at a constant value j_0 independent on look direction, especially independent on Θ, the co-latitude relative to every normal on the source surface. The different angles we are using are sketched in Fig. 9. To implement an isotropic distribution in our simulation, we set each area on the source sphere to a emit number of protons $\mathrm{d}N_i$ per solid angle, energy interval, and time:

$$\mathrm{d}N_i = (\vec{j}_0 \mathrm{d}\vec{A})(\mathrm{d}\Omega)(\mathrm{d}E\ \mathrm{d}T) = (j_0\ \mathrm{d}A\ \cos\Theta)(\sin\Theta\ \mathrm{d}\Theta\ \mathrm{d}\phi)(\mathrm{d}E\ \mathrm{d}T) \tag{14}$$

The quantity $\mathrm{d}A\ \cos\Theta$ is the effective area visible from locations described by the angle Θ. This makes $\mathrm{d}N_i$ depend on Θ even though j_0 is isotropic.

$\mathrm{d}N_i$ is linked to the physical quantity j_0 via the total number N_I of particles injected over the energy interval ΔE and over the time period ΔT.

$$N_I = \int \mathrm{d}N_i = \left(4\pi r^2 \int_0^{\pi/2} \mathrm{d}\Theta\ \cos\Theta\ \sin\Theta \int_0^{2\pi} \mathrm{d}\phi\right)\left(j_0 \int \mathrm{d}E \int \mathrm{d}T\right)$$
$$= (4\pi^2 r^2)(j_0 \Delta E\ \Delta T) \tag{15}$$

Because we did not launch particles outward of the sphere, the Θ integral in N_I only goes up to $\pi/2$. For each proton event we record the ionizing energy losses on the various LEMMS SSDs and apply the coincidence logic between SSDs that LEMMS uses to identify particle species and energy (Krimigis et al., 2004). We then count the number of particles fulfilling the logic irrespective of incidence angle. We call this number N_C, while the number of particles counted in a θ-interval is N_c. We define θ as the co-latitude relative to the boresight pointing along the axis of LEMMS. LEMMS is a double-sided telescope consisting of a LET and a HET side. The angle for particles entering the LET along the boresight is $\theta = 0°$ and 180° for the direction of the HET. Note that this angle is different to Θ measured from the source sphere normal.

With the quantities above, we can express the intensity j_0 in our simulation using the angle-averaged geometry factor G and the counted particles N_C:

$$j_0 = \frac{N_C}{G\ \Delta E\ \Delta T}, \tag{16}$$

which can be reformed using Eq. (15), yielding the geometry factor

$$G = \frac{N_C}{j_0\ \Delta E\ \Delta T} = 4\pi^2 r^2 \frac{N_C}{N_I} \tag{17}$$

Eq. (17) can also be found in Yando et al. (2011), their Eq. A7.

We also define the geometry factor g within an interval of θ, which will turn out to be useful.

$$g = \frac{N_c}{j_0\ \Delta E\ \Delta T} \tag{18}$$

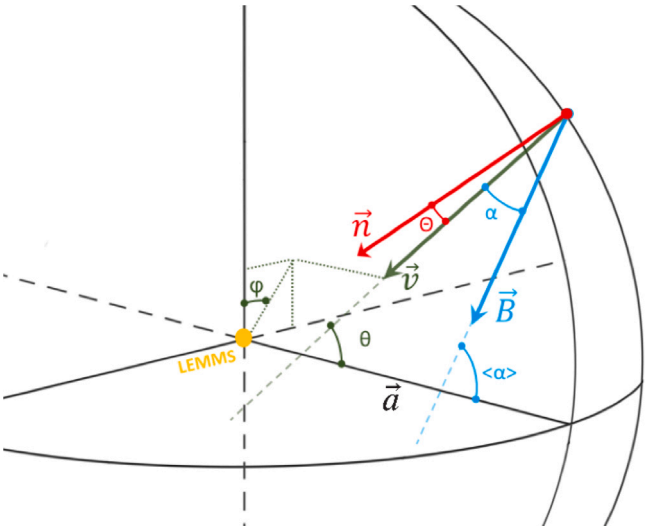

Fig. 9. Sketch illustrating the various angles used in the calculation of geometry factors and intensity inversions. The velocity vector of a particle injected in the GEANT4/GRAS simulation or measured in Saturn's radiation belts is called $\vec{v}$. The instrument boresight axis following the center of the LEMMS LET follows the vector $\vec{a}$. We use this vector to set up a coordinate system relative to the instrument. In this system, $\vec{a}$ takes the place of the polar axis in spherical coordinates and defines the co-latitude θ between $\vec{v}$ and $\vec{a}$, as well as the longitude φ. The normal of the source sphere is called $\vec{n}$, relative to which we define a co-latitude Θ. The respective longitude angle ϕ is not shown for clarity. The local magnetic field follows the vector $\vec{B}$, with α the pitch angle between the particle velocity $\vec{v}$ and the field $\vec{B}$. $\langle\alpha\rangle$ is the pitch angle between the instrument boresight $\vec{a}$ and the field $\vec{B}$.

To simplify our forward model, we replace all θ >90° values with 180°-θ, so that g becomes the total geometry factor of HET and LET combined. Separating particle access from the LET and HET is not necessary here since we are analyzing trapped radiation, for which the flux at conjugate pitch angles is the same.

The value of g alone is not meaningful without knowledge of the θ range it is associated with. We therefore define a differential geometry factor, g_d, as

$$g_d = \frac{g}{\Delta\Omega} = \frac{\pi r^2}{(\cos\theta_1 - \cos\theta_2)} \frac{N_c}{N_I} \tag{19}$$

where $\Delta\Omega$ is the solid angle over the interval θ_1 to θ_2 and over all φ. It is given as

$$\Delta\Omega = 2\int_{\theta_1}^{\theta_2} \mathrm{d}\theta\ \sin\theta \int_0^{2\pi} \mathrm{d}\varphi = 4\pi(\cos\theta_1 - \cos\theta_2) \tag{20}$$

The angle φ is the longitude relative to the instrument boresight axis. The factor 2 is necessary because we defined g as the addition of LET and HET. The division with this $\Delta\Omega$ turns g_d into the average of LET and HET with $g_d(\theta) = g_d(180° - \theta)$.

Values for g_d are shown in Fig. 3. An equivalent expression to Eq. (19) can be found in Selesnick et al. (2017), their Eq. (2) without derivation.

A.3. Average responses

The differential geometry factor g_d used here is related to the commonly used angular-averaged geometry factor G as

$$G = 2\int \mathrm{d}\Omega\ g_d\ = 2\int_0^{2\pi} \mathrm{d}\varphi \int_0^{\pi/2} \mathrm{d}\theta\ g_d\ \sin\theta \tag{21}$$

G is still energy dependent. If an instrument channel has a well defined nominal response over a narrow energy range ΔE it can be useful to calculate the effective geometry factor

$$\langle G\rangle = \frac{\int_{E_1}^{E_2} G\ \mathrm{d}E}{\Delta E} \tag{22}$$

and use it to approximate the intensity via $j \approx R/(\Delta E\ \langle G\rangle)$ (Eq. (1)).

Sometimes it can be useful to calculate an integral intensity I, the number of particles coming from all directions beyond a threshold energy E_0.

$$I = \int_0^{\pi} \mathrm{d}\alpha \int_{E_0}^{\infty} \mathrm{d}E\ j(E,\alpha) \tag{23}$$

I can be estimated from instrument channels that are integral and respond to all energies above a certain energy E_0. For such channels we can calculate $\langle G\rangle$ as the average value of G beyond E_0 and approximate $I \approx R/\langle G\rangle$. We have shown such an estimated integral intensity in Fig. 1 to get a first overview of the data in roughly instrument-independent units.

A.4. Discussion

We find that the nominal response of channels that show a nominal response to a narrow energy range (e.g. P1–P6) that is consistent with previously used values for G (Armstrong et al., 2009), as already discussed earlier (Roussos et al., 2018b). Several other channels (e.g. P7–P9, E7) were found to not respond to the nominal range they were designed for. Their response was checked for consistency with measurements of Earth's radiation belts.

The inclusion of the static magnetic field in the LET assembly allowed us to reasonably extend the energy range of instrument response down to 10 keV, where the magnet has a strong influence. We find that the response of the A channels (used in channel set 1) and C channels (not used in this work) shows G values that are consistent with what has been used before. The new values are 1.5–3 times smaller, which we attribute to the lower fidelity modeling done earlier.

Generally, the magnet may also have an effect on higher energies due to its effect on the secondary particles produced within the instrument. However, our simulations indicate that for the energy range of interest the effect of the permanent magnets is small nevertheless. The strongest effect is seen in a slightly stronger penetrator response of LET at energies > 5 GeV (e.g. channels P7, P8, E7 in Fig. 3), presumably because primary protons with such high energies have a large yield of creating lower energy secondaries at different passive shielding elements of LEMMS which the LET magnetic field subsequently focuses on the SSDs.

For these highest energy protons considered here (≈ 1 GeV), a comparison of LEMMS GCR measurements with precision GCR spectra by terrestrial observatories indicate an underestimation of the omnidirectional LEMMS geometric factors values by factors less than 5 (e.g. 3–4 for channel E7) (Roussos et al., 2020b, 2019), which may introduce a small systematic overestimation of the absolute fluxes estimated around those energies, but not in a different spectral shape.

We currently neglect the spacecraft when calculating the LEMMS response. We anticipate that the spacecraft may lower g_d at each energy by a maximum factor of 2 for penetrating protons. This can happen because Cassini may stop penetrating ions and their secondaries from about half of the sky and the respective φ-values before they reach LEMMS. LEMMS itself has roughly cylindrical symmetry (except for particles responding to its magnetic field). Any residual asymmetry should cause a weaker φ-dependence of its response than the maximum modification by the spacecraft. We ignore any such small variability here because we use geometry factors that average over φ (e.g. Eq. (20)).

Appendix B. Forward modeling details

With Eq. (2) we provided a relation between the expected count rate R_f^i based on an assumed spectrum $j(E,\alpha,\lambda^i)$. We reproduce this equation here for easier reference and number it as Eq. (24).

$$R_f^i\left(\langle\alpha\rangle^i,\lambda^i\right) = \int_0^{\pi}\mathrm{d}\theta\int_0^{2\pi}\mathrm{d}\varphi\int_0^{\infty}\mathrm{d}E\ j(E,\alpha,\lambda^i)\ g_d(E,\theta,\varphi)\ \sin(\theta) \tag{24}$$

Originally we describe the spectrum as $j(\alpha_{eq},E)$ (Eq. (4)). In order to evaluate Eq. (24), we therefore need to know how α_{eq} relates to the angles α, θ, and φ. This will be described in this section.

Most straightforward is the relation between equatorial and local pitch angle of the particle, which follows from the conservation of the first adiabatic invariant.

$$\alpha_{eq}\left(\alpha,\lambda\right) = \arcsin\left(\sqrt{\frac{B_{eq}}{B(\lambda)}}\sin\alpha\right) \tag{25}$$

Eq. (24) integrates over θ and φ, which describe the direction of the particle locally and near the instrument, relative to the instrument boresight, as sketched in Fig. 9. We therefore need to relate every combination of θ and φ to $\langle\alpha\rangle$, the local pitch angle into which the instrument boresight is pointing to. The relation can be derived from the cosine law on a sphere, as for example given in Li et al. (2013), their Eq. (4).

$$\alpha(\theta,\varphi,\langle\alpha\rangle) = \arccos[\cos\langle\alpha\rangle\ \cos\theta + \sin\langle\alpha\rangle\ \sin\theta\ \cos\varphi], \tag{26}$$

When doing these calculations it is important to keep in mind that the two pitch angles α (describing the particle) and $\langle\alpha\rangle$ (describing the instrument) are generally not the same. They are arbitrarily different when the particle enters through the shielding. When the particle enters through the center of the nominal opening of the telescope, they are mirrored around 90° or identical, when only considering the 0 to 90° range. However, most particles will not enter through the center. So while at a given time we keep $\langle\alpha\rangle$ fixed, we still need to scan over a range of α values (and equivalent θ and φ angles).

What is left is relating the local pitch angle of the instrument to the respective equatorial pitch angle, which works formally the same way as for the pitch angle of the particle:

$$\langle\alpha\rangle\left(\langle\alpha_{eq}\rangle,\lambda\right) = \arcsin\left(\sqrt{\frac{B(\lambda)}{B_{eq}}}\sin\langle\alpha_{eq}\rangle\right) \tag{27}$$

Appendix C. Trapping limit

Magnetic trapping breaks down if the magnetic field changes significantly over a nominal gyromotion.

The gyroradius r_g in a constant field is

$$r_g = \frac{p\sin(\alpha)}{qB} \tag{28}$$

with the momentum p, the local pitch angle α, the charge q of the particle, and the absolute magnetic field B.

The gyroradius needs to be compared a scale length l of the change of the total magnetic field, which is defined as

$$l = \frac{B}{|\vec{\nabla}B|} \tag{29}$$

We assume that magnetic trapping breaks down for (Thomas and Doherty, 1971; Cooper et al., 2018)

$$\eta = \frac{r_g}{l} = \frac{1}{8} \tag{30}$$

We calculate $|\vec{\nabla}B|$ in a dipole field. A dipole magnetic field in spherical coordinates with coordinates in radius r, co-latitude from the north pole θ, and longitude ϕ is (Walt, 1994)

$$\vec{B} = \left(\frac{-2B_sR_s^3\ \cos\theta}{r^3}, \frac{-B_sR_s^3\ \sin\theta}{r^3}, 0\right) \tag{31}$$

B_s and R_s are the surface magnetic field and radius at the equator of the respective planet.

The absolute value of the dipole field is

$$B = B_s\left(\frac{R_s}{r}\right)^3 T \tag{32}$$

with $T = \sqrt{3(\cos\theta)^2 + 1}$. Note that r is still the radial distance, not the L-shell.

Now we first calculate the gradient vector of the absolute value of B. (The gradient of the vector $\vec{B}$ is zero for all fields.)

$$\vec{\nabla} B = \left(\frac{\partial B}{\partial r}, \frac{1}{r}\frac{\partial B}{\partial \theta}, \frac{1}{r\sin\theta}\frac{\partial B}{\partial \phi} \right) = \left(\frac{3B_s R_s^3 T}{r^4}, \frac{3B_s R_s^3 \cos\theta \sin\theta}{r^4 T}, 0 \right) \quad (33)$$

With this we can calculate the absolute value of the gradient.

$$|\vec{\nabla} B| = \frac{3B_s R_s^3}{r^4}\sqrt{T^2 + \frac{(\cos\theta)^2(\sin\theta)^2}{T^2}} \quad (34)$$

$$\frac{1}{l} = \frac{|\vec{\nabla} B|}{B} = \frac{3}{r}\sqrt{1 + \frac{(\cos\theta)^2(\sin\theta)^2}{T^4}} \approx \frac{3}{r} \quad (35)$$

The approximation is justified because the value of the square root is between 1 and 1.03 for all θ.

Combining Eqs. (28) and (35), and using the relation $r = L\ R_s\ (\sin\theta)^2$ for a dipole field, yields

$$p = \eta \frac{qB_s R_s}{3L^2 \sin(\alpha)} \frac{\sqrt{1 + 3\cos^2(\theta)}}{\sin^4(\theta)} \quad (36)$$

where p is now the maximum momentum that can be trapped at the given pitch angle and co-latitude. The smallest trapping values at a given pitch angle are found in the equatorial plane for $\theta = 90°$. While higher momenta could be temporarily trapped at higher latitudes, their trapping will not be stable when the particles pass the equatorial plane. We can therefore set $\theta = 90°$ to calculate the trapping limit in Eq. (36).

Generally, non-equatorial pitch angles can be trapped up to higher momenta than equatorial ones. The momentum p_c until which it is possible to trap particles of all pitch angles can be calculated from Eq. (36) by setting $\alpha = 90°$.

$$p_c = \eta \frac{qB_s R_s}{3L^2} \quad (37)$$

This momentum can be converted to the trapping energy $\widetilde{E}_c$ that we use in Eq. (10).

$$\widetilde{E}_c = \sqrt{(m\ c^2)^2 + (c\ p)^2} - (m\ c^2) \quad (38)$$

where m is the particle rest mass and c the speed of light.

This analytic estimate of the trapping limit only considers the gradient of a magnetic dipole field. Curvature of the dipole can also be an issue, as well as non-dipolar field components, which is why $\widetilde{E}_c$ should be considered as an upper limit.

Appendix D. Assumed exosphere

Most details of the spectral shape resulting from CRAND have been provided earlier (Cooper et al., 2018; Cooper and Sturner, 2018). What has not been discussed are details on the assumed atmosphere, which are provided here.

We model the high altitude atmosphere above the 1-bar level until $1.17 R_S$. The atmosphere was represented through 24 slabs of gas with 60Mm width and different thicknesses. The model accounts for the exosphere and an assumed corona. The density of the respective slabs is based on what was assumed for planning the final phase of the Cassini mission (Strobel, 2015; Kollmann et al., 2018a). The dense atmosphere is accounted for by a single, dense slab at the bottom. The overall density profile of the slabs is shown in Fig. 10. The composition is hydrogen with a helium fraction of 6% at the bottom that decreases to zero at an altitude of 4000 km.

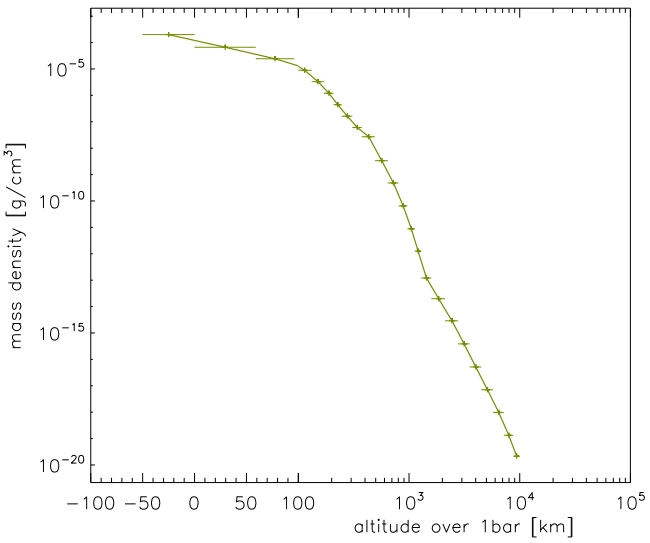

Fig. 10. Exospheric density profile assumed for the calculation of the CRAND production in the atmosphere. The altitude scale is linear below 100 km and logarithmic otherwise. Error bars along the x-axis demarcate the thickness of the slabs.

Appendix E. Numerical calculation of the physical model

The physical model of Saturn's proton belts introduced in Section 3.5 describes the phase space density f of protons as a simple 1D function depending on energy E. We assume that the protons are provided by the CRAND source $S(E)$ (Section 3.4), after which they experience cooling (Section 3.5). The respective energy loss is characterized with the energy loss per distance in material dE/dx, which is available as tabulated values (e.g. Zieger and Hansen (2008), Berger et al. (2005)) that can be scaled to the density of the respective gas. dE/dx describes a loss of energy and therefore is always negative. For completeness, we initially also assume here that particles are also lost with a lifetime τ. We formally carry this term within this appendix but will not use it when evaluating the results to get the spectra discussed in Section 3.5. The differential equation that compiles these processes is then (Schulz and Lanzerotti, 1974; Kollmann et al., 2013).

$$\frac{\partial f}{\partial t} = -\frac{v}{p^2}\frac{\partial}{\partial E}\left(p^2 f \frac{dE}{dx}\right) + S - \frac{f}{\tau} \quad (39)$$

$$= \underbrace{-\frac{v}{p^2}\left(p^2 \frac{dE}{dx}\right)}_{C}\frac{\partial f}{\partial E} + \underbrace{\left(-\frac{v}{p^2}\frac{\partial}{\partial E}\left(p^2\frac{dE}{dx}\right) - \frac{1}{\tau}\right)}_{D} f \quad (40)$$

p is the proton momentum. Eq. (40) is a first order partial differential equation, which will require one boundary condition to be solved. As a boundary we will set f at the highest energy as zero, which is approximately true for the observed spectra that fall with increasing energy. Here we will aim for a steady state solution, which means that there is no need to assume an initial condition.

Numerically we will describe the function $f(E)$ as a vector with discrete energy steps numbered with e: $\vec{f} = (..., f_e, f_{e+1}, ...)$. We will solve f for $1 \le e \le \epsilon$, where ϵ is the number of energy steps that will be solved. For clarity we will only spell out two components, e and $e+1$ from now on. We will write matrices as $\underline{A}$. By using vectors and matrices we will eventually turn the solution of Eq. (40) into a matrix inversion problem, which can be solved through standard methods. The spacing of the discrete energy steps can be energy dependent itself and shall be ΔE_e. For our model, we chose logarithmically spaced energy steps. The energy derivative is then

$$\left.\frac{\partial f}{\partial E}\right|_e = \frac{f_{e+1} - f_e}{\Delta E_e} \quad (41)$$

One element of Eq. (40) can then be written as

$$\left.\frac{\partial f}{\partial t}\right|_e = \frac{C_{e+1}+C_e}{2}\frac{f_{e+1}-f_e}{\Delta E_e} + D_e f_e + S_e \tag{42}$$

$$= \alpha_e f_e + \beta_e f_{e+1} + S_e \tag{43}$$

The equivalent vector expression is

$$\begin{pmatrix} \partial f/\partial t|_e \\ \partial f/\partial t|_{e+1} \end{pmatrix} = \underbrace{\begin{pmatrix} \alpha_e & \beta_e & 0 \\ 0 & \alpha_{e+1} & \beta_{e+1} \end{pmatrix}}_{\underline{A}_f} \underbrace{\begin{pmatrix} f_e \\ f_{e+1} \\ B \end{pmatrix}}_{\vec{f}_f+\vec{B}_f} + \underbrace{\begin{pmatrix} S_e \\ S_{e+1} \end{pmatrix}}_{\vec{S}_e} \tag{44}$$

$$= \begin{pmatrix} \alpha_e f_e + \beta_e f_{e+1} + S_e \\ \alpha_{e+1} f_{e+1} + \beta_{e+1} B + S_{e+1} \end{pmatrix}$$

$$= \underbrace{\begin{pmatrix} \alpha_e & \beta_e \\ 0 & \alpha_{e+1} \end{pmatrix}}_{\underline{A}_s} \underbrace{\begin{pmatrix} f_e \\ f_{e+1} \end{pmatrix}}_{\vec{f}_s} + \underbrace{\begin{pmatrix} 0 \\ \beta_{e+1} B \end{pmatrix}}_{\underline{A}_f \vec{B}_f} + \underbrace{\begin{pmatrix} S_e \\ S_{e+1} \end{pmatrix}}_{\vec{S}_s} \tag{45}$$

We define $B = f_{\epsilon+1}$ as the boundary condition, which we will chose as $B = 0$. The index f indicates that an array has the "full" $(\epsilon+1)\times\epsilon$ elements and a vector has $\epsilon+1$ elements. In contrast the index s will refer to "square" matrices with $\epsilon\times\epsilon$ elements and respective vectors with ϵ elements. Involving square matrices is important because eventually we will invert this matrix, which is not possible otherwise.

When assuming a steady state, $\partial f/\partial t = 0$, we can convert Eq. (45) into

$$\vec{f}_s = \underline{A}_s^{-1}\left(-\underline{A}_f \vec{B}_f - \vec{S}_s\right) \tag{46}$$

Eq. (46) turns solving the differential Eq. (40) into inverting the square matrix $\underline{A}_s$ into $\underline{A}_s^{-1}$ and applying it to a few defined vectors. We invert the matrix using the LA_INVERT procedure of the software Interactive Data Language (Harris Geospatial Solutions, 2009) that makes use of several LAPACK routines (Anderson et al., 1999). A result is shown as the red curve in the middle panel of Fig. 7.

Appendix F. Supplementary data

Supplementary material related to this article can be found online at https://doi.org/10.1016/j.icarus.2021.114795.

References

Agostinelli, S., et al., 2003. Geant4 - a simulation toolkit. Nuc. Instr. Meth. 506, 250–303.

Allegrini, F., Mauk, B., Clark, G., Gladstone, G., Hue, V., Kurth, W., Bagenal, F., Bolton, S., Bonfond, B., Connerney, J.E.P., Ebert, R.W., Greathouse, T., Imai, M., Levin, S., Louarn, P., McComas, D.J., Saur, J., Szalay, J.R., Valek, P.W., Wilson, R.J., 2020. Energy flux and characteristic energy of electrons over jupiter's main auroral emission. J. Geophys. Res. (Space Physics) 125 (4), e27693. http://dx.doi.org/10.1029/2019JA027693.

Anderson, E., Bai, Z., Bischof, C., Blackford, S., Demmel, J., Dongarra, J., Du Croz, J., Greenbaum, A., Hammarling, S., McKenney, A., Sorensen, D., 1999. LAPACK Users' Guide. SIAM.

Armstrong, T., Taherion, S., Manweiler, J., Krimigis, S., Paranicas, C., Mitchell, D., Krupp, N., 2009. Energetic ions trapped in saturn's inner magnetosphere. Planet. Space Sci. 57, 1723–1731. http://dx.doi.org/10.1016/j.pss.2009.03.008.

Bagenal, F., Wilson, R.J., Siler, S., Paterson, W.R., Kurth, W.S., 2016. Survey of galileo plasma observations in jupiter's plasma sheet. J. Geophys. Res. (Planets) 121, 871–894. http://dx.doi.org/10.1002/2016JE005009.

Becker, H.N., Alexander, J.W., Connerney, J.E.P., Brennan, M.J., Guillaume, A., Adumitroaie, V., Florence, M.M., Kollmann, P., Mauk, B.H., Bolton, S.J., 2021. High latitude zones of GeV heavy ions at the inner edge of jupiter's relativistic electron belt. J. Geophys. Res. Planets 126 (5), http://dx.doi.org/10.1029/2020JE006772, e2020JE006772, URL: https://agupubs.onlinelibrary.wiley.com/doi/abs/10.1029/2020JE006772.

Berger, M.J., Coursey, J.S., Zucker, M.A., Chang, J., 2005. Stopping-power and range tables for electrons, protons, and helium ions. http://www.nist.gov/physlab/data/star.

Blake, J.B., Hilton, H.H., Margolis, S.H., 1983. On the injection of cosmic ray secondaries into the inner saturnian magnetosphere. I - Protons from the CRAND process. J. Geophys. Res. 88, 803–807. http://dx.doi.org/10.1029/JA088iA02p00803.

Buratti, B.J., Thomas, P.C., Roussos, E., Howett, C., Seiß, M., Hendrix, A.R., Helfenstein, P., Brown, R.H., Clark, R.N., Denk, T., Filacchione, G., Hoffmann, H., Jones, G.H., Khawaja, N., Kollmann, P., Krupp, N., Lunine, J., Momary, T.W., Paranicas, C., Postberg, F., Sachse, M., Spahn, F., Spencer, J., Srama, R., Albin, T., Baines, K.H., Ciarniello, M., Economou, T., Hsu, H.W., Kempf, S., Krimigis, S.M., Mitchell, D., Moragas-Klostermeyer, G., Nicholson, P.D., Porco, C.C., Rosenberg, H., Simolka, J., Soderblom, L.A., 2019. Close cassini flybys of saturn's ring moons pan, daphnis, atlas, pandora, and epimetheus. Science 364, eaat2349. http://dx.doi.org/10.1126/science.aat2349.

Clark, G., Paranicas, C., Santos-Costa, D., Livi, S., Krupp, N., Mitchell, D.G., Roussos, E., Tseng, W.-L., 2014. Evolution of electron pitch angle distributions across Saturn's middle magnetospheric region from MIMI/LEMMS. Planet. Space Sci. 104, 18–28. http://dx.doi.org/10.1016/j.pss.2014.07.004.

Cooper, J.F., 1983. Nuclear cascades in saturn's rings - cosmic ray albedo neutron decay and origins of trapped protons in the inner magnetosphere. J. Geophys. Res. 88, 3945–3954. http://dx.doi.org/10.1029/JA088iA05p03945.

Cooper, J.F., Johnson, R.E., Kollmann, P., Roussos, E., Sittler, E.C., 2018. Plasma, neutral atmosphere, and energetic radiation environments of planetary rings. In: Tiscareno, M.S., Murray, C.D. (Eds.), Planetary Ring Systems: Properties, Structure, and Evolution. In: Cambridge Planetary Science, Cambridge University Press, pp. 363–398. http://dx.doi.org/10.1017/9781316286791.014.

Cooper, J.F., Sturner, S.J., 2018. Energetic radiation from galactic cosmic ray interactions with saturn's main rings. J. Geophys. Res. Space Phys. 123, http://dx.doi.org/10.1029/2018JA025583, URL: https://agupubs.onlinelibrary.wiley.com/doi/abs/10.1029/2018JA025583.

Dialynas, K., Brandt, P.C., Krimigis, S.M., Mitchell, D.G., Hamilton, D.C., Krupp, N., Rymer, A.M., 2013. The extended saturnian neutral cloud as revealed by global ENA simulations using cassini/MIMI measurements. J. Geophys. Res. (Space Physics) 118 (6), 3027–3041. http://dx.doi.org/10.1002/jgra.50295.

Dougherty, M.K., Cao, H., Khurana, K.K., Hunt, G.J., Provan, G., Kellock, S., Burton, M.E., Burk, T.A., Bunce, E.J., Cowley, S.W.H., Kivelson, M.G., Russell, C.T., Southwood, D.J., 2018. Saturn's magnetic field revealed by the cassini grand finale. Science 362 (6410), http://dx.doi.org/10.1126/Science.aat5434.

Fennell, J.F., Claudepierre, S.G., Blake, J.B., O'Brien, T.P., Clemmons, J.H., Baker, D.N., Spence, H.E., Reeves, G.D., 2015. Van allen probes show that the inner radiation zone contains no MeV electrons: ECT/MagEIS data. Geophys. Res. Lett. 42 (5), 1283–1289. http://dx.doi.org/10.1002/2014GL062874, URL: https://agupubs.onlinelibrary.wiley.com/doi/abs/10.1002/2014GL062874.

Fleshman, B.L., Delamere, P.A., Bagenal, F., Cassidy, T., 2012. The roles of charge exchange and dissociation in spreading saturn's neutral clouds. J. Geophys. Res. 117, 5007. http://dx.doi.org/10.1029/2011JE003996, arXiv:1204.0979.

Glass, G., Jain, M., Evans, M.L., Hiebert, J., Northcliffe, L.C., Bonner, B.E., Simmons, J.E., Bjork, C., Riley, P., Cassapakis, C., 1977. Neutron spectra at 0deg from proton-proton collisions between 647 and 805 MeV. Phys. Rev. D 15, 36–46. http://dx.doi.org/10.1103/PhysRevD.15.36.

Goldhagen, P., Reginatto, M., Kniss, T., Wilson, J.W., Singleterry, R.C., Jones, I.W., Van Steveninck, W., 2002. Measurement of the energy spectrum of cosmic-ray induced neutrons aboard an ER-2 high-altitude airplane. Nuc. Instr. Meth. 476, 42–51. http://dx.doi.org/10.1016/S0168-9002(01)01386-9.

Harris Geospatial Solutions, I., 2009. IDL 7.1. commerical software, https://www.harrisgeospatial.com/Software-Technology/IDL.

Hess, W.N., Patterson, H.W., Wallace, R., Chupp, E.L., 1959. Cosmic-ray neutron energy spectrum. Phys. Rev. 116, 445–457. http://dx.doi.org/10.1103/PhysRev.116.445.

Johnston, W.R., O'Brien, T.P., Huston, S.L., Guild, T.B., Ginet, G.P., 2015. Recent updates to the AE9/AP9/SPM radiation belt and space plasma specification model. IEEE Trans. Nucl. Sci. 62, 2760–2766. http://dx.doi.org/10.1109/TNS.2015.2476470.

Jurac, S., Richardson, J.D., 2005. A self-consistent model of plasma and neutrals at Saturn: Neutral cloud morphology. J. Geophys. Res. 110 (A9), 9220. http://dx.doi.org/10.1029/2004JA010635.

Kim, K.-C., Shprits, Y., 2012. Radial gradients of phase space density in the inner electron radiation. J. Geophys. Res. Space Physics 117 (A12), http://dx.doi.org/10.1029/2012JA018211, URL: https://agupubs.onlinelibrary.wiley.com/doi/abs/10.1029/2012JA018211.

Kollmann, P., Clark, G., Paranicas, C., Mauk, B., Roussos, E., Nénon, Q., Garrett, H.B., Sicard, A., Haggerty, D., Rymer, A., 2021. Jupiter's ion radiation belts inward of Europa's orbit. J. Geophys. Res. Space Phys. 126 (4), http://dx.doi.org/10.1029/2020JA028925, e2020JA028925, URL: https://agupubs.onlinelibrary.wiley.com/doi/abs/10.1029/2020JA028925, e2020JA028925.

Kollmann, P., Paranicas, C., Clark, G., Mauk, B.H., Haggerty, D.K., Rymer, A.M., Santos-Costa, D., Connerney, J.E.P., Allegrini, F., Valek, P., Kurth, W.S., Gladstone, G.R., Levin, S., Bolton, S., 2017. A heavy ion and proton radiation belt inside of Jupiter's rings. Geophys. Res. Lett. 44 (11), 5259–5268. http://dx.doi.org/10.1002/2017GL073730, URL: http://dx.doi.org/10.1002/2017GL073730, 2017GL073730.

Kollmann, P., Paranicas, C., Lagg, A., Roussos, E., Lee-Payne, Z.-H., Kusterer, M., Smith, D., Krupp, N., Vandegriff, J., 2020. Galileo/EPD user guide. http://dx.doi.org/10.1002/essoar.10503620.1, ESSOAr, http://sd-www.jhuapl.edu/Galileo_EPD/userguide/GaliUse_v25C.pdf.

Kollmann, P., Roussos, E., Kotova, A., Regoli, L., Mitchell, D.G., Carbary, J., Clark, G., Krupp, N., Paranicas, C., 2018a. Saturn's innermost radiation belt throughout and inward of the D-ring. Geophys. Res. Lett. 45, http://dx.doi.org/10.1029/2018GL077954, URL: https://agupubs.onlinelibrary.wiley.com/doi/abs/10.1029/2018GL077954.

Kollmann, P., Roussos, E., Paranicas, C., Krupp, N., Haggerty, D.K., 2013. Processes forming and sustaining saturn's proton radiation belts. Icarus 222, 323–341. http://dx.doi.org/10.1016/j.icarus.2012.10.033.

Kollmann, P., Roussos, E., Paranicas, C., Krupp, N., Jackman, C.M., Kirsch, E., Glassmeier, K.-H., 2011. Energetic particle phase space densities at Saturn: Cassini observations and interpretations. J. Geophys. Res. 116 (A15), A05222. http://dx.doi.org/10.1029/2010JA016221.

Kollmann, P., Roussos, E., Paranicas, C., Woodfield, E.E., Mauk, B.H., Clark, G., Smith, D.C., Vandegriff, J., 2018b. Electron acceleration to MeV energies at Jupiter and Saturn. J. Geophys. Res. 123 (11), 9110–9129. http://dx.doi.org/10.1029/2018JA025639.

Kollmann and Roussos, E., Kotova, A., Paranicas, C., Krupp, N., 2017. The evolution of saturn's radiation belts modulated by changes in radial diffusion. Nat. Astron. 1, 872–877. http://dx.doi.org/10.1038/s41550-017-0287-x, shared first authorship.

Kotova, A., Roussos, E., Kollmann, P., Krupp, N., Dand ouras, I., 2019. Galactic cosmic rays access to the magnetosphere of Saturn. J. Geophys. Res. (Space Physics) 124 (1), 166–177. http://dx.doi.org/10.1029/2018JA025661.

Krimigis, S.M., Armstrong, T.P., 1982. Two-component proton spectra in the inner saturnian magnetosphere. Geophys. Res. Lett. 9, 1143–1146. http://dx.doi.org/10.1029/GL009i010p01143.

Krimigis, S.M., Armstrong, T.P., Axford, W.I., Bostrom, C.O., Fan, C.Y., Gloeckler, G., Lanzerotti, L.J., 1977. The low energy charged particle (LECP) experiment on the voyager spacecraft. Space Sci. Rev. 21 (3), 329–354. http://dx.doi.org/10.1007/BF00211545.

Krimigis, S.M., Mitchell, D.G., Hamilton, D.C., Krupp, N., Livi, S., Roelof, E.C., Dandouras, J., Armstrong, T.P., Mauk, B.H., Paranicas, C., Brandt, P.C., Bolton, S., Cheng, A.F., Choo, T., Gloeckler, G., Hayes, J., Hsieh, K.C., Ip, W., Jaskulek, S., Keath, E.P., Kirsch, E., Kusterer, M., Lagg, A., Lanzerotti, L.J., LaVallee, D., Manweiler, J., McEntire, R.W., Rasmuss, W., Saur, J., Turner, F.S., Williams, D.J., Woch, J., 2005. Dynamics of saturn's magnetosphere from MIMI during Cassini's orbital insertion. Science 307, 1270–1273. http://dx.doi.org/10.1126/Science.1105978.

Krimigis, S.M., Mitchell, D.G., Hamilton, D.C., Livi, S., Dandouras, J., Jaskulek, S., Armstrong, T.P., Boldt, J.D., Cheng, A.F., Gloeckler, G., Hayes, J.R., Hsieh, K.C., Ip, W.-H., Keath, E.P., Kirsch, E., Krupp, N., Lanzerotti, L., Lundgren, R., Mauk, B.H., McEntire, R.W., Roelof, E., Schlemm, C.E., Tossman, B.E., Wilken, B., Williams, D.J., 2004. Magnetosphere imaging instrument (MIMI) on the Cassini mission to Saturn/Titan. Space Sci. Rev. 114, 233–329. http://dx.doi.org/10.1007/s11214-004-1410-8.

Kronberg, E.A., Daly, P.W., 2013. Spectral analysis for wide energy channels. Geosci. Instrum. Methods Data Syst. 2 (2), 257–261. http://dx.doi.org/10.5194/gi-2-257-2013, URL: https://gi.copernicus.org/articles/2/257/2013/.

Krupp, N., Kollmann, P., Mitchell, D.G., Thomsen, M., Jia, X., Masters, A., Zarka, P., 2018a. Global configuration and seasonal variations of Saturn's magnetosphere. In: Saturn in the 21st Century. In: Cambridge Planetary Science, Cambridge University Press, Cambridge, U.K., pp. 126–165. http://dx.doi.org/10.1017/9781316227220.006.

Krupp, N., Roussos, E., Kollmann, P., Mitchell, D.G., Paranicas, C.P., Krimigis, S.M., Hamilton, D.C., Hedman, M., Dougherty, M.K., 2018b. Energetic neutral and charged particle measurements in the inner saturnian magnetosphere during the grand finale orbits of cassini 2016/2017. Geophys. Res. Lett. http://dx.doi.org/10.1029/2018GL078096.

Krupp, N., Roussos, E., Lagg, A., Woch, J., Müller, A., Krimigis, S.M., Mitchell, D.G., Roelof, E.C., Paranicas, C., Carbary, J., Jones, G.H., Hamilton, D.C., Livi, S., Armstrong, T.P., Dougherty, M.K., Sergis, N., 2009. Energetic particles in saturn's magnetosphere during the Cassini nominal mission (july 2004-july 2008). Planet. Space Sci. 57, 1754–1768. http://dx.doi.org/10.1016/j.pss.2009.06.010.

Lejosne, S., Kollmann, P., 2020. Radiation belt radial diffusion at earth and beyond. Space Sci.Rev. 216 (1), 19. http://dx.doi.org/10.1007/s11214-020-0642-6.

Li, W., Ni, B., Thorne, R.M., Bortnik, J., Green, J.C., Kletzing, C.A., Kurth, W.S., Hospodarsky, G.B., 2013. Constructing the global distribution of chorus wave intensity using measurements of electrons by the POES satellites and waves by the Van Allen Probes. Geophys. Res. Lett. 40 (17), 4526–4532. http://dx.doi.org/10.1002/grl.50920, URL: http://dx.doi.org/10.1002/grl.50920.

Li, X., Selesnick, R.S., Baker, D.N., Jaynes, A.N., Kanekal, S.G., Schiller, Q., Blum, L., Fennell, J., Blake, J.B., 2015. Upper limit on the inner radiation belt MeV electron intensity. J. Geophys. Res. Space Phys. 120 (2), 1215–1228. http://dx.doi.org/10.1002/2014JA020777, URL: https://agupubs.onlinelibrary.wiley.com/doi/abs/10.1002/2014JA020777.

Lorentzen, K.R., Mazur, J.E., Looper, M.D., Fennell, J.F., Blake, J.B., 2002. Multisatellite observations of MeV ion injections during storms. J. Geophys. Res. 107, 1231. http://dx.doi.org/10.1029/2001JA000276.

Lyons, L.R., Thorne, R.M., 1973. Equilibrium structure of radiation belt electrons. J. Geophys. Res. 78 (13), 2142–2149. http://dx.doi.org/10.1029/JA078i013p02142, URL: https://agupubs.onlinelibrary.wiley.com/doi/abs/10.1029/JA078i013p02142.

Mauk, B.H., 2014. Comparative investigation of the energetic ion spectra comprising the magnetospheric ring currents of the solar system. J. Geophys. Res. 119, 9729–9746. http://dx.doi.org/10.1002/2014JA020392.

McDonald, F.B., Schardt, A.W., Trainor, J.H., 1980. If you've seen one magnetosphere, you haven't seen them all - energetic particle observations in the saturn magnetosphere. J. Geophys. Res. 85, 5813–5830. http://dx.doi.org/10.1029/JA085iA11p05813.

Nénon, Q., Sicard, A., Kollmann, P., Garrett, H.B., Sauer, S.P.A., Paranicas, C., 2018. A physical model of the proton radiation belts of Jupiter inside europa's orbit. J. Geophys. Res. 123, 3512–3532. http://dx.doi.org/10.1029/2018JA025216.

Reeves, G.D., Friedel, R.H.W., Larsen, B.A., Skoug, R.M., Funsten, H.O., Claudepierre, S.G., Fennell, J.F., Turner, D.L., Denton, M.H., Spence, H.E., Blake, J.B., Baker, D.N., 2016. Energy-dependent dynamics of kev to MeV electrons in the inner zone, outer zone, and slot regions. J. Geophys. Res. Space Phys. 121 (1), 397–412. http://dx.doi.org/10.1002/2015JA021569, URL: https://agupubs.onlinelibrary.wiley.com/doi/abs/10.1002/2015JA021569.

Roederer, J.G., 1970. Dynamics of Geomagnetically Trapped Radiation. Springer Verlag, Heidelberg, Germany.

Roussos, E., Cohen, C., Kollmann, P., Goncalves, P., Pinto, M., 2020a. Energetic heavy ions in Jupiter's innermost radiation belts: revisiting heavy ion counter data from Galileo. In: AGU Fall Meeting Abstracts, Vol. 2020. pp. SM052–0007.

Roussos, E., Dialynas, K., Krupp, N., Kollmann, P., Paranicas, C., Roelof, E.C., Yuan, C., Mitchell, D.G., Krimigis, S.M., 2020b. Long- and short-term variability of galactic cosmic-ray radial intensity gradients between 1 and 9.5 au: Observations by cassini, BESS, BESS-polar, PAMELA, and AMS-02. Astrophys. J. 904 (2), 165. http://dx.doi.org/10.3847/1538-4357/abc346.

Roussos, E., Jackman, C.M., Thomsen, M.F., Kurth, W.S., Badman, S.V., Paranicas, C., Kollmann, P., Krupp, N., Bučík, R., Mitchell, D.G., Krimigis, S.M., Hamilton, D.C., Radioti, A., 2018a. Solar energetic particles (SEP) and galactic cosmic rays (GCR) as tracers of solar wind conditions near saturn: Event lists and applications. Icarus 300, 47–71. http://dx.doi.org/10.1016/j.icarus.2017.08.040.

Roussos, E., Jones, G.H., Krupp, N., Paranicas, C., Mitchell, D.G., Lagg, A., Woch, J., Motschmann, U., Krimigis, S.M., Dougherty, M.K., 2007. Electron microdiffusion in the saturnian radiation belts: Cassini MIMI/LEMMS observations of energetic electron absorption by the icy moons. J. Geophys. Res. 112 (A11), 6214. http://dx.doi.org/10.1029/2006JA012027.

Roussos, E., Kollmann, P., 2021. The radiation belts of Jupiter and Saturn. In: Space Physics and Aeronomy, Magnetospheres in the Solar System. Wiley, arXiv:2006.14682, URL: https://arxiv.org/abs/2006.14682, 2020045732.

Roussos, Kollmann, P., Krupp, N., Kotova, A., Regoli, L., Paranicas, C., Mitchell, D.G., Krimigis, S.M., Hamilton, D., Brandt, P., Carbary, J., Christon, S., Dialynas, K., Dandouras, I., Hill, M.E., Ip, W.H., Jones, G.H., Livi, S., Mauk, B.H., Palmaerts, B., Roelof, E.C., Rymer, A., Sergis, N., Smith, H.T., 2018b. A radiation belt of energetic protons located between Saturn and its rings. Science 362 (6410), aat1962. http://dx.doi.org/10.1126/science.aat1962, shared first authorship, URL: http://science.sciencemag.org/content/362/6410/eaat1962.

Roussos, E., Kollmann, P., Krupp, N., Paranicas, C.P., Dialynas, K., Jones, G., Mitchell, D.G., Krimigis, S.M., Cooper, J.F., 2018c. Sources, sinks and transport of energetic electrons near Saturn's main rings. Geophys. Res. Lett. http://dx.doi.org/10.1029/2018GL078097, URL: https://agupubs.onlinelibrary.wiley.com/doi/abs/10.1029/2018GL078097.

Roussos, E., Krupp, N., Armstrong, T., Paranicas, C., Mitchell, D.G., Krimigis, S.M., Jones, G.H., Dialynas, K., Sergis, N., Hamilton, D.C., 2008. Discovery of a transient radiation belt at Saturn. Geophys. Res. Lett. 35, 22106. http://dx.doi.org/10.1029/2008GL035767.

Roussos, E., Krupp, N., Dialynas, K., Kollmann, P., Paranicas, C., Echer, E., Mitchell, D.G., Krimigis, S.M., 2019. Jovian cosmic-ray protons in the heliosphere: Constraints by Cassini observations. Astrophys. J. 871 (2), 223. http://dx.doi.org/10.3847/1538-4357/aafb2f.

Roussos, E., Krupp, N., Paranicas, C.P., Kollmann, P., Mitchell, D.G., Krimigis, S.M., Armstrong, T.P., Went, D.R., Dougherty, M.K., Jones, G.H., 2011. Long- and short-term variability of Saturn's ionic radiation belts. J. Geophys. Res. 116 (A15), A02217. http://dx.doi.org/10.1029/2010JA015954.

Rymer, A.M., Mauk, B.H., Hill, T.W., Paranicas, C., Mitchell, D.G., Coates, A.J., Young, D.T., 2008. Electron circulation in Saturn's magnetosphere. J. Geophys. Res. 113 (A12), 1201. http://dx.doi.org/10.1029/2007JA012589.

Santin, G., Ivanchenko, V., Evans, H., Nieminen, P., Daly, E., 2005. GRAS: a general-purpose 3-D modular simulation tool for space environment effects analysis. IEEE Trans. Nucl. Sci. 52 (6), 2294–2299. http://dx.doi.org/10.1109/TNS.2005.860749.

Sauer, H.H., 1980. On Saturnian cosmic ray cutoff rigidities. Geophys. Res. Lett. 7, 215–217. http://dx.doi.org/10.1029/GL007i003p00215.

Schulz, M., Lanzerotti, L.J., 1974. Particle diffusion in the radiation belts. In: Roederer, J. (Ed.), Physics and Chemistry in Space, Vol. 7, first ed. Springer Verlag, Heidelberg, Germany.

Selesnick, R.S., Albert, J.M., 2019. Variability of the proton radiation belt. J. Geophys. Res. Space Phys. 124 (7), 5516–5527. http://dx.doi.org/10.1029/2019JA026754, URL: https://agupubs.onlinelibrary.wiley.com/doi/abs/10.1029/2019JA026754.

Selesnick, R.S., Baker, D.N., Kanekal, S.G., Hoxie, V.C., Li, X., 2017. Modeling the proton radiation belt with van allen probes relativistic electron-proton telescope data. J. Geophys. Res. http://dx.doi.org/10.1002/2017JA024661, 2017JA024661.

Selesnick, R.S., Blake, J.B., 2000. On the source location of radiation belt relativistic electrons. J. Geophys. Res. 105, 2607–2624. http://dx.doi.org/10.1029/1999JA900445.

Selesnick, R.S., Hudson, M.K., Kress, B.T., 2010. Injection and loss of inner radiation belt protons during solar proton events and magnetic storms. J. Geophys. Res. Space Phys. 115 (A8), http://dx.doi.org/10.1029/2010JA015247, URL: https://agupubs.onlinelibrary.wiley.com/doi/abs/10.1029/2010JA015247.

Selesnick, R.S., Hudson, M.K., Kress, B.T., 2013. Direct observation of the CRAND proton radiation belt source. J. Geophys. Res. 118, 7532–7537. http://dx.doi.org/10.1002/2013JA019338.

Selesnick, R.S., Looper, M.D., Mewaldt, R.A., 2007. A theoretical model of the inner proton radiation belt. Space Weather 5, 4003. http://dx.doi.org/10.1029/2006SW000275.

Shemansky, D.E., Liu, X., Melin, H., 2009. The Saturn hydrogen plume. Planet. Space Sci. 57, 1659–1670. http://dx.doi.org/10.1016/j.pss.2009.05.002.

Singer, S.F., 1958. Trapped albedo theory of the radiation belt. Phys. Rev. Lett. 1, 181–183. http://dx.doi.org/10.1103/PhysRevLett.1.181.

Strobel, D., 2015. Update of SAMWG proximal mission planning: modeling Saturn's upper atmosphere. Saturn Atmosphere Working Group Presentation.

Thomas, J., Doherty, W.R., 1971. Calculations of neutron-decay-proton trapping in the Jovian magnetosphere. In: Proceedings of the Jupiter Radiation Belt Workshop, Vol. JPL Technical Memorandum 33-543. (19720020200), pp. 315–347, URL: https://ntrs.nasa.gov/citations/19720020200.

Usoskin, I.G., Alanko-Huotari, K., Kovaltsov, G.A., Mursula, K., 2005. Heliospheric modulation of cosmic rays: Monthly reconstruction for 1951–2004. J. Geophys. Res. 110 (A9), 12108. http://dx.doi.org/10.1029/2005JA011250.

Van Allen, J.A., 1984. Energetic particles in the inner magnetosphere of Saturn. In: Gerhels, T., Matthews, M. (Eds.), Saturn. The University of Arizona Press, Tucson, Arizona, pp. 281–317.

Van Allen, J.A., Frank, L.A., 1959. Radiation around the earth to a radial distance of 107,400 km.. Nature 183, 430–434. http://dx.doi.org/10.1038/183430a0.

Vandegriff, J., DiFabio, R., Hamilton, D., Kusterer, M., Manweiler, J., Mitchell, D., Paranicas, C., Roussos, E., 2018. Cassini/MIMI instrument data user guide. NASA's planetary data system, http://cassini-mimi.jhuapl.edu/documents/mimi_user_guide_9_26_18.pdf.

Vay, J.-L., 2008. Simulation of beams or plasmas crossing at relativistic velocity. Phys. Plasmas 15 (5), 056701. http://dx.doi.org/10.1063/1.2837054.

Walt, M., 1994. Introduction To Geomagnetically Trapped Radiation, first ed. Cambridge University Press, Cambridge, United Kingdom.

Yando, K., Millan, R.M., Green, J.C., Evans, D.S., 2011. A Monte Carlo simulation of the NOAA POES medium energy proton and electron detector instrument. J. Geophys. Res. 116, A10231. http://dx.doi.org/10.1029/2011JA016671.

Zhelavskaya, I.S., Aseev, N.A., Shprits, Y.Y., 2021. A combined neural network and physics based approach for modeling plasmasphere dynamics. J. Geophys. Res. (Space Physics) 126 (3), e28077. http://dx.doi.org/10.1029/2020JA028077.

Zieger, B., Hansen, K.C., 2008. Statistical validation of a solar wind propagation model from 1 to 10 AU. J. Geophys. Res. 113, 8107. http://dx.doi.org/10.1029/2008JA013046.